

# The Globally Coherent Pattern of Autumn Monsoon Precipitation

Nandini Ramesh\*, Quentin Nicolas

*Department of Earth and Planetary Science, University of California, Berkeley, California*

William R. Boos

*Department of Earth and Planetary Science, University of California, Berkeley, California*

*Climate and Ecosystem Sciences Division, Lawrence Berkeley National Laboratory, Berkeley, California*

\*Corresponding author: Nandini Ramesh, nandiniramesh@berkeley.edu.

## ABSTRACT

Over most tropical land areas, the annual peak in precipitation occurs during summer, associated with the local monsoon circulation. However, in some coastal regions in the tropics the bulk of annual precipitation occurs in autumn, after the low-level summer monsoon westerlies have abated. Examples include the Nordeste region of Brazil, southeastern India and Sri Lanka, and coastal Tanzania. Unlike equatorial regions, they receive little rainfall during local spring. Such regions are present along the eastern coasts of nearly all continents, suggesting that they comprise a coherent yet previously unrecognized global phenomenon.

In this study, we identify eight tropical locations that experience an “autumn monsoon” and show that this unusual seasonal cycle is generated by similar mechanisms in all of these. When these regions receive their peak rainfall, they lie poleward of the ITCZ in easterly low-level winds. The spatial structure of precipitation in these regions can be explained by their placement to the east of mountain ranges that organize moist convection on their windward sides. However, orographic forcing alone cannot explain their unique seasonal cycle: despite similarities in wind direction, surface humidity, and sea surface temperatures (SSTs) between autumn and spring, these regions receive significantly more rainfall in autumn than in spring. We show that this is due to differences in the large-scale atmospheric stability between the equinoctial seasons, which can be captured by a relative SST metric and is influenced by SSTs in the remote eastern upwelling zones of the Pacific and Atlantic Oceans.

<sup>27</sup> **1. Introduction**

<sup>28</sup> Land regions throughout the tropics typically experience peak rainfall during summer, associated  
<sup>29</sup> with monsoon circulations on each landmass. However, on multiple continents, areas exist where  
<sup>30</sup> most of the annual precipitation occurs in autumn or winter, and the summer is relatively dry.  
<sup>31</sup> Unlike locations close to the equator that experience two rainy seasons in spring and autumn, these  
<sup>32</sup> regions receive comparatively little precipitation during spring.

<sup>33</sup> A well-studied example of such a location is the Nordeste region of Brazil, where the wet season  
<sup>34</sup> occurs in austral autumn. In South Asia, the autumn rainfall peak is referred to as the northeast  
<sup>35</sup> monsoon, retreating monsoon, or post-monsoon, and is the primary source of rainfall for southeast-  
<sup>36</sup> ern peninsular India and northeastern Sri Lanka. There are also regions that receive much of their  
<sup>37</sup> annual precipitation during local autumn in East Africa, Southeast Asia, and Central America.

<sup>38</sup> Figure 1 displays the climatological fraction of total annual rainfall received during autumn and  
<sup>39</sup> winter in the tropics of each hemisphere. Regions that receive half or more of their annual rainfall  
<sup>40</sup> in these months (September to February in the Northern Hemisphere, or March to August in the  
<sup>41</sup> Southern Hemisphere) are typically narrow strips along the eastern coasts of landmasses or island  
<sup>42</sup> chains. In most cases, they are located to the east and equatorward of the summer monsoon regions  
<sup>43</sup> on each continent.

<sup>44</sup> In previous studies that classified the tropics into climatic regimes, these regions have either been  
<sup>45</sup> categorized as semiarid savannas or grouped with summer monsoon regions (Ramage et al. 1971;  
<sup>46</sup> Wang 1994; Zhang and Wang 2008; Beck et al. 2018), possibly due to the relatively low spatial  
<sup>47</sup> resolution of historical precipitation data. However, the unusual seasonal cycle of these regions  
<sup>48</sup> has long been known, as noted in the book *The Earth's Problem Climates* (Trewartha 1961), which  
<sup>49</sup> refers to an annual “summer drought” in several of these areas when cataloguing the locations

50 on each continent with climatological characteristics that do not conform to those of their sur-  
51 roundings. Most of these areas are densely populated, and some have historical records detailing  
52 drought-induced famines of devastating intensity, including Brazil's Nordeste region, southeastern  
53 India, the island of Luzon in the Philippines, and southern coastal Kenya (Davis 2002). Despite the  
54 striking similarities between the climates of these regions, they have not previously been considered  
55 as a unified phenomenon or climate regime with comparable physical drivers. In this study, we  
56 propose on the basis of observed features and physical arguments that these regions constitute a  
57 single climate type or regime, generated by similar mechanisms.

58 *a. Review of studies of individual regions*

59 Although no work has proposed a unified view of all of these regions, the annual cycle and  
60 variability of precipitation in many of these locations have been examined in regional studies.  
61 Below, we summarize these existing studies.

62 Of the autumn monsoon regions, the case that has received perhaps the most attention is the  
63 Nordeste region of Brazil (Hastenrath 2012), an area that typically receives its peak rainfall in  
64 April, i.e., austral autumn, in contrast with the summer (December-February) peak in rainfall  
65 experienced by most of the South American landmass in the Southern Hemisphere. This region  
66 is prone to severe droughts known as *secas* that have had pronounced socioeconomic impacts,  
67 resulting in famines and mass migrations out of the region (Greenfield 2001; Davis 2002;  
68 Aceituno et al. 2009), and is home to large urban centers such as Recife and Salvador. The  
69 timing of the annual rainfall peak in the northern part of this region has been attributed to the  
70 location of the Intertropical Convergence Zone (ITCZ) in the Atlantic sector, which reaches the  
71 southernmost point in its annual migration in March and April (Hastenrath 2012); we will show  
72 that additional factors play a significant role. The interannual variability here is closely related to

<sup>73</sup> El Niño-Southern Oscillation (ENSO) (Pezzi and Cavalcanti 2001), which influences the timing of  
<sup>74</sup> the ITCZ's meridional movement via the Atlantic sea surface temperature (SST) gradient (Nobre  
<sup>75</sup> and Shukla 1996; Uvo et al. 1998; Giannini et al. 2004).

<sup>76</sup> In the Northern Hemisphere, the Maracaibo region of northern Venezuela and Colombia similarly  
<sup>77</sup> experiences an autumn peak in rainfall, in contrast with surrounding summer-monsoon regions  
<sup>78</sup> (Pulwarty et al. 1992), and is heavily influenced by tropical Pacific SSTs (Lyon 2003). Parts  
<sup>79</sup> of the Caribbean coast of Central America, including northern Honduras (Portig 1965) and the  
<sup>80</sup> flood-prone Mexican state of Tabasco (Aparicio et al. 2009), also receive most of their rainfall in  
<sup>81</sup> autumn.

<sup>82</sup> A number of eastern coastal regions in the Indo-Pacific display a similar seasonal cycle. In South  
<sup>83</sup> Asia, the autumn rainfall peak over densely populated, southeastern peninsular India and Sri  
<sup>84</sup> Lanka provides a crucial source of water for rice cultivation (referred to as the *rabi* and *maha*  
<sup>85</sup> crops, respectively, in these two countries; Singh and Sontakke 1999; Zubair 2002). This rainfall is  
<sup>86</sup> highly variable on interannual timescales: both flooding due to excessive rainfall (van Oldenborgh  
<sup>87</sup> et al. 2016; Kumaran et al. 2020) and droughts (Guha-Sapir et al. 2016) have afflicted the region  
<sup>88</sup> in recent years. ENSO is a key modulator of this variability (Suppiah 1989; Zubair 2002; Kumar  
<sup>89</sup> et al. 2006), along with SSTs in the Indian Ocean (Zubair et al. 2003; Kripalani and Kumar 2004;  
<sup>90</sup> Yadav 2013). Similarly to the Nordeste region of Brazil, it has been hypothesized that the ITCZ's  
<sup>91</sup> meridional movement determines the timing and amount of rainfall over this part of the world  
<sup>92</sup> (Yadav 2013; Gadgil 2018).

<sup>93</sup> Figure 1 shows that parts of the Maritime Continent and Southeast Asia receive most of their  
<sup>94</sup> rainfall in autumn and winter. Exceptions to the general pattern of summer rainfall maxima in this  
<sup>95</sup> region have been noted in several studies (e.g. Wang 1994; Chang et al. 2004, 2005). Of these  
<sup>96</sup> exceptions, coastal central Vietnam and the eastern halves of the Malay Peninsula and Philippines

97 stand out as locations that receive significantly more rainfall in autumn and winter than in spring  
98 and summer (Chang et al. 2005; Robertson et al. 2011), and the latter two of these have been  
99 described as northward extensions of the Australian summer monsoon (Robertson et al. 2011).  
100 Although boreal fall and winter are the seasons when most tropical cyclone activity occurs in  
101 this region, the precipitation associated with tropical cyclones typically contributes only a small  
102 fraction of the total seasonal rainfall there (Chen et al. 2012; Bagtasa 2017). Numerous studies  
103 have pointed out that the transitions between the Asian and Australian summer monsoons are  
104 not symmetric: the ITCZ moves southwards gradually from Asia to Australia over the course  
105 of boreal autumn, but abruptly shifts northwards from Australia to Asia in boreal spring (Wang  
106 1994; Aldrian and Susanto 2003; Hung et al. 2004; Chang et al. 2005; Zhang and Wang 2008).  
107 Consequently, the boreal autumn and winter months bring a peak in rainfall to a few locations in  
108 the Maritime Continent that are north of the equator, but equivalent regions on the other side of  
109 the equator that receive peak rainfall in austral autumn and winter are far less extensive. This is  
110 consistent with Figure 1, which shows that the eastern coastal regions of Australia and the island  
111 of New Guinea do not receive receive more rainfall in local autumn and winter than in spring and  
112 summer. One hypothesis for the mechanism producing this asymmetry is that the Pacific Walker  
113 cell, which is maintained by the zonal SST gradient across the equatorial Pacific, is strongest in  
114 boreal autumn due to enhanced upwelling in the eastern equatorial Pacific at this time of year  
115 producing cool SSTs, leading to increased ascent over the Maritime Continent (Wang 1994; Li and  
116 Philander 1996). A later hypothesis, put forward by Chang et al. (2005) and explored in model  
117 experiments by Wang and Chang (2008), proposes that the high heat capacity of the oceans leads  
118 to warmer SSTs in autumn following the peak summer insolation, leading to increased convection  
119 at this time of year.  
120 At the other end of the Indian Ocean basin, the Tanzanian and southern Kenyan coastline receives

maximum precipitation in the austral autumn months of April and May. This rainy season is known locally as the *masika* or “long rains,” and is the primary source of rainfall for major population centers such as Dar Es Salaam and Mombasa. Much of East Africa experiences a season of “long rains” during austral autumn and “short rains” during austral spring, but the coastal section of East Africa in the Southern Hemisphere is the only area where the *masika* rains comprise more than half of the annual rainfall (Hastenrath et al. 2011; Yang et al. 2015; Gamoyo et al. 2015). The region is highly vulnerable to variations in this rainfall: shortfalls have led to famines in greater East Africa (e.g. Lyon and DeWitt 2012), and excessive rainfall has produced flooding in Dar Es Salaam in recent years (Guha-Sapir et al. 2016).

130

### 131 b. *Goals and approach*

132 In this study, we examine the mechanisms that generate the autumn rainfall peak in all of the regions discussed above and provide evidence that they comprise an analogous phenomenon on various continents, driven by similar processes.

135 We begin by examining the spatial distribution of regions in the tropics that receive most of their annual rainfall in autumn and winter, as opposed to summer (Section 3). We find strong parallels between these regions in terms of the timing of the annual precipitation peak and their alignment with the eastern margins of landmasses. We then investigate three factors that typically affect the annual cycle of tropical precipitation. The first is the seasonal movement of the ITCZ: as summer monsoons on each continent end, the ITCZ moves equatorward in autumn, possibly producing peak rainfall in locations that lie equatorward of nearby summer monsoon regions (Section 4). We find that this does not explain the autumn monsoon pattern, as the autumn monsoon regions do not lie within the main ITCZ during the months of peak rainfall; instead, they manifest as narrow

<sup>144</sup> protrusions from the main rainband into the autumn hemisphere. A significant feature associated  
<sup>145</sup> with the seasonal movement of the ITCZ is the reversal of the prevailing winds from westerly  
<sup>146</sup> during local summer, when the ITCZ is poleward of the autumn monsoon regions, to easterly  
<sup>147</sup> during the months of peak precipitation. These easterly winds and the proximity of the autumn  
<sup>148</sup> monsoon regions to mountain ranges lead us to consider the second factor: the interaction of winds  
<sup>149</sup> with orography to produce rainfall (Section 5). We find that orographic effects broadly explain  
<sup>150</sup> the spatial distribution of rainfall in autumn, especially the alignment of autumn monsoon regions  
<sup>151</sup> along eastern coasts, but do not provide accurate estimates of the rainfall amount or of the annual  
<sup>152</sup> cycle. The third factor we investigate is the role of moist convection. Using a budget analysis,  
<sup>153</sup> we show that horizontal moisture convergence associated with deep, convectively coupled ascent  
<sup>154</sup> above orography in these regions is responsible for the large rainfall amounts observed during  
<sup>155</sup> autumn (Section 6). Further, we find that the effects of local and remote SSTs, particularly in  
<sup>156</sup> eastern ocean upwelling zones, play a key role in setting the atmospheric conditions that promote  
<sup>157</sup> moist convection in autumn (Section 7). We summarize our results and their implications in  
<sup>158</sup> Section 8.

<sup>159</sup>

## <sup>160</sup> 2. Data and Methods

<sup>161</sup> We use multiple observational and reanalysis data sets, all of which are publicly available.  
<sup>162</sup> Table 1 lists the name, resolution, geographic coverage, time period, and variables used for each  
<sup>163</sup> data set. All data used is at monthly resolution. Where variables from different data sources are  
<sup>164</sup> shown together, climatologies and other quantities are calculated for the overlapping set of years.  
<sup>165</sup> Our figures and analysis are produced using two precipitation estimates: TRMM and CHIRPS,  
<sup>166</sup> which have differing temporal coverage and spatial resolution. Importantly, CHIRPS only contains

<sup>167</sup> data over land, whereas TRMM contains data over both land and ocean. In computing time  
<sup>168</sup> series or other spatial averages, the averaging is performed within the boxes shown in Figure 3  
<sup>169</sup> with areas outside the 0.5 contour in these figures masked to exclude regions that receive less  
<sup>170</sup> than half of their annual rainfall in autumn and winter. Smaller boxes shown in Figures 1, 4, 5,  
<sup>171</sup> and 6 contain the same masked land area as those shown in Figure 3 and were used for visualization.

<sup>172</sup>

### <sup>173</sup> **3. The Climatological Distribution of Tropical Autumn Precipitation**

<sup>174</sup> Figure 1 displays the climatological fraction of annual rainfall over tropical land regions during  
<sup>175</sup> autumn and winter in each hemisphere, here defined as September to February for the Northern  
<sup>176</sup> Hemisphere and March to August for the Southern Hemisphere, computed using the CHIRPS data.  
<sup>177</sup> Regions that receive most of their annual rainfall in summer (shaded blue) cover most of this map,  
<sup>178</sup> consistent with the dominant role played by summer monsoon circulations in producing rainfall  
<sup>179</sup> over tropical land. Most regions that receive half or more of their annual rainfall during autumn  
<sup>180</sup> and winter (shaded orange and red) are along the eastern coasts of continents and in many cases  
<sup>181</sup> lie equatorward of a large summer monsoon region.

<sup>182</sup> We select the following eight eastern coastal regions (highlighted by boxes in Figure 1) that receive  
<sup>183</sup> most of their annual rainfall in autumn and winter for analysis in this study:

- <sup>184</sup> 1. Central America: northern Honduras and the coast of Tabasco in Mexico.
- <sup>185</sup> 2. Venezuela: the Maracaibo region of northern Venezuela and Colombia.
- <sup>186</sup> 3. South Asia: eastern Sri Lanka and the southeastern Indian state of Tamilnadu.
- <sup>187</sup> 4. Malay Peninsula: the southeastern edge of the Malay Peninsula.
- <sup>188</sup> 5. Vietnam: central coastal Vietnam.

- <sup>189</sup> 6. Philippines: the eastern half of the Philippines.
- <sup>190</sup> 7. Brazil: northeastern coastal Brazil, known as the Nordeste region.
- <sup>191</sup> 8. Tanzania: coastal Tanzania and a portion of the coast of southern Kenya.
- <sup>192</sup> We exclude regions with less than 2 mm/day in annual-mean rainfall such as the coast of the Horn  
<sup>193</sup> of Africa and parts of the Middle East, as well as a few islands in the Maritime Continent and  
<sup>194</sup> Caribbean. Figure 2 shows the mean annual cycle for each of the eight regions listed, averaged  
<sup>195</sup> over the areas in Figure 1 that receive half or more of their annual rainfall in autumn and winter.  
<sup>196</sup> The annual cycle of precipitation in these regions displays a remarkably similar pattern consisting  
<sup>197</sup> of a large peak in rainfall during late autumn or early winter (October-December for the Northern  
<sup>198</sup> Hemisphere and March-April for the Southern Hemisphere), with a smaller peak during late  
<sup>199</sup> spring or early summer that may be associated with rainfall received during the summer monsoon  
<sup>200</sup> in adjacent regions. The large rainfall peak that occurs in these regions during late autumn and  
<sup>201</sup> early winter, which we will refer to as the autumn monsoon, is the subject of this study.
- <sup>202</sup> Figure 3 shows the climatological rainfall over ocean and land from TRMM during October-  
<sup>203</sup> December in the Northern Hemisphere and April-June in the Southern Hemisphere, with the gray  
<sup>204</sup> contour encompassing regions that receive more than half their annual precipitation in autumn  
<sup>205</sup> and winter, and stippling indicating other regions. Over the global tropics, most rainfall during  
<sup>206</sup> these months occurs over the ocean, with only a relatively small land area receiving rainfall.  
<sup>207</sup> Figure 3 also highlights the coastal nature of many of the autumn monsoon regions and their  
<sup>208</sup> proximity to areas of high precipitation over the ocean. A few other eastern coastal regions, such  
<sup>209</sup> as southeastern Papua New Guinea and the eastern coast of Madagascar, also receive substantial  
<sup>210</sup> amounts of rainfall during this season, but not enough to comprise more than 50% of the year's  
<sup>211</sup> total rainfall.

212 In Figure 4, the climatological month of maximum precipitation, after a 5-month running mean is  
213 applied, is shown based on CHIRPS data. An interesting feature is the relative scarcity of regions  
214 with a spring peak (shown in shades of red-orange in the Northern Hemisphere and violet in the  
215 Southern Hemisphere) compared with regions that receive their peak rainfall in autumn (violet in  
216 the Northern Hemisphere, red-orange in the Southern Hemisphere). Further, the few regions with  
217 a spring peak that do exist do not align systematically with eastern coastlines, unlike regions with  
218 an autumn peak. Despite the similar insolation received and the prevailing easterly wind direction  
219 in these seasons, an asymmetry exists over the global tropics between spring and autumn that  
220 favors precipitation along eastern coastlines during autumn. The origin of this asymmetry is a key  
221 question that will be explored in later sections of this paper.

222 A prominent feature in Figure 4 is the meridional migration of the ITCZ over the continents of  
223 Africa and South America. From south to north on these continents, the month of maximum  
224 precipitation progresses through the calendar from austral summer (shades of blue) to boreal  
225 summer (shades of orange-yellow), reflecting the migration of the ITCZ from the austral to  
226 boreal summer monsoon regions, which cover most of the map. The broad zonal strips over  
227 equatorial Africa and South America with peaks in the equinoctial seasons are a consequence of  
228 this migration. These regions experience two peaks in their annual cycle that are of near equal  
229 magnitude (Wang 1994), unlike the autumn monsoon regions shown in Figure 2.

230 The delayed peak in rainfall, as well as the location of many of the autumn monsoon regions  
231 equatorward of the summer monsoon regions, point to the possibility that they receive their peak  
232 rainfall in autumn due to the movement of the ITCZ over these areas. This hypothesis has been  
233 advanced in studies of two of these regions: Northeastern Brazil (e.g. Nobre and Shukla 1996;  
234 Hastenrath 2012) and southeastern India (Gadgil 2018). In the following section, we explore the  
235 timing of the ITCZ's seasonal meridional movement as a possible explanation for the autumn peak

236 in precipitation at these locations.

237

#### 238 **4. Seasonal Cycle of the ITCZ and Winds**

239 On monthly timescales, the ITCZ lags the latitude of maximum insolation (Waliser and Gautier  
240 1993; Hu et al. 2007), meaning that in many parts of the globe, it is at its most poleward position  
241 towards the end of local summer, rather than during the solstices. The offset in the timing of peak  
242 rainfall between summer and autumn monsoon regions could thus arise from movement of the  
243 ITCZ: as the summer monsoon ends, the ITCZ and the latitude of maximum precipitation shift  
244 equatorward in autumn.

245 Figure 5 shows the movement of the ITCZ over spring and fall. The percentiles of outgoing  
246 longwave radiation (OLR) with respect to the distribution of OLR over the tropics (20°S-20°N)  
247 are shown for November and May, with the lowest percentiles indicating the main centers of  
248 deep convective activity in those months. The ITCZ location, represented by the centroid of  
249 precipitation at each longitude, is depicted as a colored line for each autumn month in each  
250 hemisphere. These lines, which cross the regions of convective activity, illustrate the migration of  
251 the ITCZ away from the poles over the course of autumn.

252 Most of the autumn monsoon regions do not lie directly beneath the ITCZ during their rainy  
253 season: instead, they lie poleward of the main ITCZ at this time of year. Partial exceptions to this  
254 general pattern are the Tanzanian coast, over which the ITCZ passes during austral autumn; the  
255 Malay Peninsula, which lies beneath the ITCZ in early boreal autumn but not during the months  
256 of peak precipitation; and the northern, but not eastern, portion of the Brazilian region. A narrow  
257 poleward protrusion of the precipitation contours (shown in white) extends over each of the autumn  
258 monsoon regions during the months shown. Robertson et al. (2011) described this phenomenon

259 over the Maritime Continent as a northward extension of the southern summer monsoon; here we  
260 note that this feature is not unique to that region and can be seen over multiple continents.

261 Figure 5, therefore, indicates that meridional movement of the ITCZ over autumn does not explain  
262 the autumn rainfall maximum seen in these regions. The ITCZ instead lies equatorward of these  
263 regions during the local autumn precipitation peak.

264 Another significant change that occurs during this time of year in the tropics is the shift in wind  
265 direction that accompanies the end of the summer monsoons. During summer, when the ITCZ over  
266 land is far from the equator, most monsoon regions experience westerly, poleward winds. As the  
267 ITCZ shifts equatorwards, surface winds revert to the easterly, equatorward direction characteristic  
268 of the Trade Winds over most of the year. During autumn, therefore, these regions experience  
269 northeasterlies and southeasterlies in the Northern and Southern Hemispheres respectively.

270 Since the peak annual precipitation in the autumn monsoon regions does not occur at the time  
271 of year when the large-scale ITCZ passes over them, and because they lie eastward of mountain  
272 ranges during periods of easterly winds, we next investigate the possible role of orographic forcing  
273 in producing the rainfall peak.

274

## **5. An Estimate of the Orographic Contribution to Autumn Monsoon Precipitation**

276 Figure 6 depicts winds 10 m above the surface during autumn in each Hemisphere, along with  
277 the topography. As expected, winds are easterly over most of the tropics, including all eight of  
278 the autumn monsoon regions. The alignment of the poleward extensions of the rain band seen in  
279 Figure 5 with eastern coastlines and their placement on the eastern edges of topographic features  
280 (see Figure 6) suggest that the prevailing easterly winds, carrying moist air from tropical oceans,  
281 are forced to ascend by orography, producing condensation and precipitation on the windward side

282 of these mountain ranges. This possibility is further supported by the spatial pattern of autumn  
283 precipitation in Figure 3, where it can be seen that many autumn monsoon regions are aligned  
284 with a nearby mountain range. Since the autumn monsoon regions lie to the east of topographic  
285 features, orographic effects may also be responsible for the lack of precipitation received in these  
286 regions during summer, when they lie on the lee of mountains in low-level westerlies associated  
287 with nearby summer monsoons.

288 We now estimate the rainfall that could be generated by upslope ascent forced by orography and  
289 compare the results with observed climatological precipitation.

290 A few simple models have been proposed for estimating the rainfall produced by orographic  
291 forcing (Rhea and Grant 1974; Smith 1979; Alpert and Shafir 1989; Sinclair 1994; Roe 2005).  
292 These models assume that air parcels rise parallel to the sloping surface as winds impinge upon the  
293 side of a mountain range; therefore, the precipitation produced is proportional to the wind speed  
294 in the direction normal to the mountain range, the slope of Earth’s surface, and the moisture in the  
295 air parcels that are lifted in the upslope flow. While the different models vary in how they account  
296 for the amount of moisture involved in producing precipitation, this proportionality is central to all  
297 of them (Smith 2018). We use the model formulated by Smith (1979) and Roe (2005), which was  
298 argued to broadly capture climatological patterns of precipitation over spatial scales larger than  
299 a few kilometers. This model assumes that condensation removes any supersaturation in rising  
300 parcels, and that ascent at every vertical level is equal to the near-surface value set by laminar,  
301 convectively stable upslope flow. The latter assumption neglects mountain wave dynamics, but the  
302 vertical wavelengths of any such waves may be sufficiently long, relative to the water vapor scale  
303 height, to render this an acceptable approximation (see discussion by Kirshbaum et al. 2018). The  
304 model rain rate  $r$  is then

$$r = \rho_0 q_0 (\mathbf{u}_0 \cdot \nabla z_s) \quad (1)$$

305 where  $\rho_0$  is the surface air density,  $q_0$  is the specific humidity of surface air (assumed equal to the  
306 specific humidity and thus the saturation specific humidity at the lifted condensation level),  $\mathbf{u}_0$  is  
307 the horizontal surface wind velocity, and  $z_s$  is surface elevation.

308 Roe (2005) further approximates the saturation humidity of surface air in terms of the sea level  
309 value of that quantity and a water vapor scale height, but we do not take that step. By assuming that  
310 all condensed moisture falls as precipitation on the windward side of the orography, Equation (1)  
311 assumes a precipitation efficiency of unity and neglects microphysical delays. In this sense it  
312 constitutes an upper bound on the rainfall produced by upslope flow, but it does not account for  
313 the possibility of additional rainfall generated by convection that may be triggered by orographic  
314 lifting.

315 Figure 7 displays the seasonal mean rain rates estimated using Equation (1) for each of the regions  
316 in autumn. For comparison, the autumn seasonal mean precipitation from observations is also  
317 shown for each region. In all cases, the model predicts some rainfall in the vicinity of the autumn  
318 monsoon regions (demarcated by the red contour), but substantially underestimates seasonal-mean  
319 precipitation over a large area in each region. It only predicts large rain rates in grid cells  
320 immediately adjacent to the mountain ranges, which in many cases (Central America, Venezuela,  
321 Philippines, Tanzania) lie further inland than the coastal region that experiences an autumn  
322 maximum in precipitation. That deficiency could be remedied by smoothing the distribution of  
323  $z_s$  used in the model to crudely represent upstream blocking, but there are other problems with  
324 the model's results. In regions such as South Asia, the Malay Peninsula, and northern Brazil, the  
325 model predicts very little rainfall in autumn. When averaged spatially within the contour for each  
326 region, the predicted rainfall amount is much lower than observed in most cases, with only the  
327 estimate in Vietnam being realistic.

328 In Figure 8, we examine the model's predicted climatological annual cycle of precipitation

over land in the autumn monsoon regions, along with each of the contributing factors: wind speed perpendicular to the orographic slope (i.e.,  $(\mathbf{u}_0 \cdot \nabla z_s)/|\nabla z_s|$ ) and surface humidity ( $q_0$ ). When compared with Figure 2, it is clear that this model of orographic rainfall, in addition to underestimating the rainfall amount, fails to describe the seasonal cycle of rainfall. The month of peak rainfall is only accurately predicted in the Philippines and nearly predicted in Vietnam: in most cases, the peak rainfall is predicted to be not in autumn but in winter or early spring, and in the Central American region, a summer peak is predicted. Inspection of the input variables reveals that the large winter peaks arise primarily from the component of the wind velocity normal to the orography. These winter peaks in easterly, equatorward wind speeds represent the lower branch of the winter Hadley Cell. Although the near-surface specific humidity falls rapidly during winter, this change is not large enough to prevent the model from predicting a winter peak in precipitation. While this suggests that the model might perhaps make a more accurate prediction if the specific humidity were accounted for differently, an examination of the seasonal cycle of specific humidity in these regions indicates otherwise: four of the regions (South Asia, Vietnam, Philippines, and Malaysia) show a peak in surface specific humidity during spring that is larger than that in autumn, meaning that if the dependence on surface specific humidity were amplified the timing of the rainfall peak would still be incorrect. This further raises the question of why, when the surface specific humidity is high and the wind direction is favorable, a large precipitation rate does not occur in these regions during spring.

These results indicate that while a model of convectively stable upslope flow can roughly explain the spatial pattern of autumn monsoon rainfall, this simple model does not explain the quantity of autumn rainfall or the timing of the rainfall peak. It is perhaps not surprising that a model of stable upslope flow would inaccurately describe orographic precipitation in the tropics, where deep moist convection can be influenced strongly by orography (e.g. Smith 1979). Such orographic

353 influence has been studied mostly in summer months (e.g. Medina et al. 2010), but it is clear  
354 that even mountain ranges only 1-2 km high can produce strong seasonal-mean precipitation  
355 maxima (Grossman and Durran 1984; Xie et al. 2006) by altering pre-existing disturbances  
356 (Houze 2012) and, perhaps, by convectively destabilizing the atmosphere (Kirshbaum et al. 2018).  
357 The systematic underestimation of rainfall by the above model of stable upslope flow, in spite  
358 of the assumed perfect precipitation efficiency, implies that ascent and thus horizontal moisture  
359 convergence are amplified by other processes.

360 We show in the following section that this amplification occurs above the orography with vertical  
361 structures suggestive of a role played by moist convection.

362

## 363 6. Moisture Budgets

364 We calculate moisture budgets for each autumn monsoon region by applying the methodology  
365 of Seager and Henderson (2013) to climatological monthly mean data from ERA5. The vertically  
366 integrated moisture convergence (VIMC) should equal the difference between precipitation ( $P$ )  
367 and evaporation ( $E$ ), i.e.:

$$P - E = -\frac{1}{\rho_w g} \nabla \cdot \int_0^{p_s} \mathbf{u} q \, dp \quad (2)$$

368 where  $\rho_w$  is the density of liquid water,  $g$  is the acceleration due to gravity,  $\mathbf{u}$  is the wind  
369 velocity along pressure surfaces,  $q$  is the specific humidity,  $p$  is pressure and the subscript  $s$   
370 denotes the surface value. The transient storage term is assumed to be negligible on monthly and  
371 seasonal timescales. Although reanalyses do not have closed moisture budgets due to assimilation  
372 tendencies, we begin by comparing climatological precipitation in each autumn monsoon region  
373 from ERA5 with that estimated from TRMM (Figure 9). In all cases, ERA5 reproduces the timing  
374 and quantity of precipitation well, with the possible exception of the Philippines, where the annual

375 peak in rainfall is slightly underestimated. The climatologies of surface evaporation and VIMC  
376 provided in ERA5, with monthly means of the latter obtained from hourly data, are also shown.  
377 The seasonal cycle of VIMC closely resembles that of precipitation, as the evaporation term varies  
378 little over the year and is comparatively small. The VIMC computed from climatological monthly  
379 mean winds and humidities nearly perfectly reproduces that provided in the reanalysis, confirming  
380 that moisture convergence by submonthly transients may be neglected when analyzing the annual  
381 cycle of precipitation in these regions.

382 The right-hand side of Equation (2) is then decomposed:

$$-\frac{1}{\rho_w g} \nabla \cdot \int_0^{p_s} \mathbf{u} q \, dp = -\frac{1}{\rho_w g} \int_0^{p_s} q \nabla \cdot \mathbf{u} \, dp - \frac{1}{\rho_w g} \int_0^{p_s} \mathbf{u} \cdot \nabla q \, dp - \frac{1}{\rho_w g} q_s u_s \cdot \nabla p_s \quad (3)$$

383 On the right-hand side of this equation, the first term represents the component of VIMC that arises  
384 due to the convergence of winds (referred to henceforth as the convergence term), the second term  
385 represents the component due to horizontal moisture advection (the advection term), and the final  
386 term represents the contribution from flow along surface pressure gradients (the surface term).

387 Physically, the surface term includes moisture convergence produced by stable upslope flow, and  
388 can be converted into the upslope flow model of Section 5 by using hydrostatic balance to transform  
389 from pressure to height coordinates.

390 Figure 10 displays the annual cycle of these terms in each region. The annual peak in the  
391 convergence term in all cases coincides with or is within a month of the annual peak in ERA5  
392 rainfall, indicating its importance in determining the annual cycle of precipitation in these regions.

393 In two of the regions – Vietnam and the Philippines – the surface term also makes a significant  
394 contribution, consistent with the prediction of the upslope flow model in the previous section. An  
395 additional feature that all of the regions have in common is that the advection term is negative  
396 during autumn, indicating that these regions lie downstream of climatologically drier areas.

397 The convergence term is influenced by the wind divergence and by the humidity, both of which are  
 398 typically related to convective activity. This, however, does not provide a causal explanation of the  
 399 seasonal cycle, as the increase in the convergence term may arise from changes in the wind field or  
 400 in humidity. To identify the contributions of these factors, we perform a Reynolds decomposition  
 401 of the moisture convergence,

$$\nabla \cdot \langle \mathbf{u}q \rangle = \nabla \cdot \langle \bar{\mathbf{u}}\bar{q} \rangle + \nabla \cdot \langle \mathbf{u}'\bar{q} \rangle + \nabla \cdot \langle \bar{\mathbf{u}}q' \rangle + \nabla \cdot \langle \mathbf{u}'q' \rangle \quad (4)$$

402 where for the quantity  $x$ ,  $\langle x \rangle$  denotes  $-\frac{1}{\rho_w g} \int_0^{p_s} x dp$ ,  $\bar{x}$  is its annual mean, and  $x'$  is the deviation  
 403 of the climatological monthly mean from the annual mean. The monthly mean values of each term  
 404 during the month of maximum climatological precipitation are shown for the autumn monsoon  
 405 regions in Table 2. In all cases, the seasonal variation in moisture convergence is dominated by  
 406 the term containing the deviation of velocity from its annual mean, i.e.,  $\nabla \cdot \langle \mathbf{u}'\bar{q} \rangle$ . This indicates  
 407 that it is not anomalous moisture in relatively steady flow that is responsible for the autumn  
 408 peak in rainfall, but that changes in the divergent wind field (i.e. ascent) primarily control the  
 409 timing of rainfall. The analysis of Section 5 showed that ascent induced by stable upslope flow  
 410 was not sufficient to explain the observed autumn rainfall, suggesting a role for convectively  
 411 coupled ascent. In the following section, we examine the vertical motion in these regions and the  
 412 large-scale forcings that may induce it.

413

## 414 7. Factors Influencing Moist Convection

415 Figure 11 displays the annual cycles of vertical mass flux (colors) and relative humidity  
 416 (contours) of the atmospheric column averaged over each of the autumn monsoon regions (the  
 417 mass flux is the ERA5 pressure-coordinate vertical velocity divided by  $g$ ). In all eight regions,

418 there is ascent and high relative humidity throughout the column during the months of peak  
419 rainfall, suggesting the presence of deep convection. This vertical mass flux is associated with  
420 the convergence term of Equation (3) and the monthly variations of the wind field, i.e.,  $\nabla \cdot \langle \mathbf{u}' \bar{q} \rangle$   
421 in Equation (4), which dominate the annual cycle. In many cases, peak ascent during the rainy  
422 season occurs in the lower troposphere, below approximately 700 hPa. Exceptions to this typical  
423 profile are found in the Indo-Pacific's Malay Peninsula and South Asia, where the vertical mass  
424 flux peaks near 300 hPa – characteristic of the broader Indo-Pacific Warm Pool region. Peak  
425 ascent over the Venezuelan region is in the mid-troposphere near 500 hPa.

426 As seen in previous sections, ascent in all regions has a seasonal cycle and autumn magnitude that  
427 cannot be explained primarily by stable upslope ascent of the Trade winds (e.g. Figure 8 and the  
428 surface term in Figure 10). The observed autumn ascent must be stronger and, in some regions  
429 (South Asia, the Malay Peninsula, and Venezuela), more top-heavy than one would expect from  
430 such an upslope flow model. Two partial exceptions to this are Vietnam and the Philippines, where  
431 very bottom-heavy ascent (Figure 11 d, f) is consistent with the surface term both accounting for  
432 a large fraction of autumn rainfall and having a high-amplitude seasonal cycle in phase with the  
433 autumn peak (Figure 10 d, f). Nevertheless, even in Vietnam and the Philippines, the total moisture  
434 convergence in the autumn peak is roughly twice that contributed by the surface term. The central  
435 question is thus what drives the magnitude and seasonal cycle of ascent seen in Figure 11.

436 A prominent feature of Figure 11 is the large differences in ascent between the autumn rainy season  
437 and early spring/late winter, with both relative humidity and ascent near their annual minimum  
438 through much of the column in the latter period. The asymmetry in rainfall between spring and  
439 autumn has been previously studied in the Maritime Continent (Hung et al. 2004; Chang et al.  
440 2005; Wang and Chang 2008; Robertson et al. 2011). Chang et al. (2005) hypothesized that this  
441 asymmetry may occur due to the high heat capacity of the ocean: after peak insolation is received

in summer, the ocean retains the energy received for a few months, causing the sea surface to be on average warmer in autumn than in spring. Continents poleward of the Maritime Continent, due to the low heat capacity of the land surface, experience similar temperatures in spring and autumn, giving rise to a stronger meridional pressure gradient in autumn than in spring that results in more precipitation over the Maritime Continent. In a subsequent study, Wang and Chang (2008) tested this hypothesis using imposed SSTs in a general circulation model and was able to reproduce features of the observed spatial pattern of precipitation in these seasons in the Maritime Continent. At a more global scale, it has long been noted that the mean latitude of the ITCZ lags that of maximum insolation (e.g. Waliser and Gautier 1993; Hu et al. 2007). This lag has been explained using similar arguments in idealized models: warmer SSTs in autumn than in spring, due to the ocean's high heat capacity, cause the ITCZ to remain in the autumn hemisphere until the onset of the summer monsoon in the other hemisphere (Xian and Miller 2008; Wei and Bordoni 2018). While the analysis in Section 4 shows that the autumn monsoon regions do not lie directly beneath the main ITCZ, this is a possible explanation for why convection is favored in these regions in autumn: SSTs peak in these regions at that time of year.

To assess whether this mechanism operates over autumn monsoon regions, we examine the seasonal cycle of SSTs in these regions (Figure 12). While the months of maximum SST do occur in autumn in some of these locations (those in the Atlantic sector and Tanzania), the mechanism outlined above cannot provide an explanation for half of the cases, particularly in the Indo-Pacific, where maximum local SSTs occur in spring rather than autumn. This suggests that local surface temperatures alone do not determine the occurrence of the precipitating ascent that produces autumn rainfall. The seasonal cycle of near-surface humidity over land strongly resembles that of local SSTs (compare with Figure 8), indicating that this behavior is not confined to ocean regions alone: the months of peak near-surface humidity over land are not the months of peak rainfall.

466 Recognizing that low-latitude ascent is not controlled by local SST alone, we assess the favorability  
467 of large-scale conditions for deep convection by examining the relative SST (RSST), calculated as  
468 the difference between local SST and SST spatially-averaged over the global tropics (20°S-20°N).  
469 The underlying argument for using RSST is that the temperature of the upper troposphere in the  
470 tropics, which is relatively spatially uniform (Sobel and Bretherton 2000), is set by the spatially  
471 averaged SST (Sobel et al. 2002) on timescales longer than approximately one month. Therefore,  
472 for conditions to facilitate convection at a given location, the SST at that location must be warm  
473 relative to that of other tropical regions, i.e., the RSST must be positive to reduce the stability of  
474 the column. RSST has proven useful in a range of contexts as an indicator of the large-scale forcing  
475 for deep convection, including in assessing the effects of anthropogenic climate change (Johnson  
476 and Xie 2010), characterizing ENSO variability (Williams and Patricola 2018), and estimating the  
477 probability of tropical cyclone formation (Vecchi and Soden 2007; Ramsay and Sobel 2011).  
478 Izumo et al. (2020) demonstrated the effectiveness of RSST in predicting the spatial pattern of  
479 tropical oceanic rainfall using monthly-mean data. Unlike convective available potential energy  
480 (CAPE), which is rapidly consumed by convective activity and therefore not a reliable indicator of  
481 the conditions promoting or suppressing convection over timescales longer than a few days, RSST  
482 remains comparatively stable over monthly timescales, providing a useful proxy for the influence  
483 of surface forcings and free-tropospheric temperature on the annual cycle of moist convection.  
484 Figure 12 shows that RSST peaks in the season of maximum rainfall and maximum ascent in each  
485 region, with the exception of the Philippines. In the Philippines, the maximum RSST occurs in  
486 local summer, when the wind direction is such that this autumn monsoon region lies on the lee  
487 of nearby mountains; this is consistent with upslope winds and the surface term making a larger  
488 contribution to the seasonal cycle of rainfall there. In all other cases, however, the RSST is highest  
489 in autumn, indicating that this is the season most favorable for moist convection in these regions.

490 While the timing of peaks and troughs of RSST is similar to that of SST in some regions (those in  
491 the Atlantic sector and Tanzania), in the Indo-Pacific sector, the shape of the RSST curve differs  
492 substantially from that of the SST curve, with RSST and SST peaks occurring nearly six months  
493 apart. To understand this discrepancy between the annual cycles of RSST and SST, we examine  
494 the seasonal cycle of tropical mean SST (i.e., the term subtracted from the local SST to arrive at  
495 the RSST) in Figure 13.

496 Tropical-mean SST peaks in boreal spring, with substantially cooler temperatures in boreal  
497 autumn. Local SSTs thus need to be higher during boreal spring to force convection than during  
498 the rest of the year. In the autumn monsoon regions in the vicinity of the Warm Pool, SST  
499 variations over the course of the year are small (Figure 12). Peak SSTs during boreal spring in  
500 these regions are not warm enough to facilitate convection during the months of the year with the  
501 highest tropical mean SST; however, during autumn when the tropical-mean SST is lower, local  
502 SSTs are sufficient to enable convection. In contrast, in the Northern Hemisphere regions in the  
503 Atlantic sector and in the Southern Hemisphere regions, RSST and SST both peak during local  
504 autumn, i.e., the amplitude of the seasonal cycle of local SSTs is large enough that subtracting the  
505 tropical-mean SST does not produce a change in the timing of the peak RSST.

506 We further investigate the seasonal cycle of tropical-mean SST in Panel (b) of Figure 13, which  
507 shows the difference in seasonal mean SST between spring and autumn. Blue regions indicate  
508 cooler SSTs in boreal autumn, and orange regions indicate warmer SSTs in boreal autumn. The  
509 largest absolute values, reaching 4-5°C, are found over the eastern cold tongues in the equatorial  
510 Pacific and Atlantic Oceans. These features, which are characterized by upwelling at the equator  
511 and eastern boundaries of ocean basins, exist due to Ekman pumping induced by prevailing  
512 easterly winds. The seasonal cycle of the oceanic ITCZ subjects large swaths of the tropical oceans  
513 to southeasterly winds in boreal autumn, intensifying the upwelling of cool subsurface waters that

514 occurs throughout the year; northeasterlies in boreal spring suppress this upwelling and raise SSTs  
515 (Li and Philander 1996, 1997). We hypothesize that these large upwelling zones therefore stabilize  
516 the zonal-mean troposphere in boreal spring, explaining the lack of a phenomenon similar to the  
517 autumn monsoon in spring in the Northern Hemisphere. A related hypothesis was outlined in  
518 Wang (1994) to explain the drier boreal spring than autumn months in the Maritime Continent  
519 region: cooler SSTs over the eastern equatorial Pacific intensify the zonal SST gradient across the  
520 Indo-Pacific during boreal autumn, thereby strengthening the Walker circulation and enhancing  
521 convection in the region during these months compared to boreal spring. The mechanism we  
522 propose applies more broadly to the entire tropics, with the most pronounced effect on the  
523 Indo-Pacific where the amplitude of the annual cycle of SSTs is small.

524 The RSST alone does not, however, provide a complete explanation of the timing of the rainfall  
525 peak: although the tropical-mean SST is lowest in August, and many of the regions thus  
526 have positive RSST, the westerly wind direction at this time of year places all of the Northern  
527 Hemisphere autumn monsoon regions on the lee of mountain ranges. In the Philippines, this effect  
528 dominates and upslope flow seems to exert a stronger control on rainfall. There is a smaller offset  
529 between the RSST and precipitation peaks over Vietnam which is likely due to the same reason.  
530 Therefore, the timing of peak rainfall in these regions depends not only on the local RSST but also  
531 on the wind direction with respect to topography.

532

## 533 8. Summary and Discussion

534 We have identified eight eastern coastal tropical regions on multiple continents that experience  
535 their primary rainfall season during local autumn. This sets them apart from most land regions  
536 in the tropics, which experience maximum rainfall during summer as part of a local monsoon

537 circulation. Despite the high population density of these coastal areas, the annual cycle of their  
538 precipitation has received relatively little attention, and they have not previously been considered  
539 as part of a unified global phenomenon. We observe several common features shared by these  
540 regions despite their geographic separation:

- 541 1. They lie on the eastern margins of landmasses, and are typically narrow.
- 542 2. They lie in close proximity to long mountain ranges of modest height.
- 543 3. They receive most of their annual rainfall in late autumn, and experience a substantially smaller  
544 rainfall peak in late spring or summer.
- 545 4. Winds in these regions are easterly and equatorward during the months of maximum precipi-  
546 tation.
- 547 5. They do not lie directly beneath the ITCZ during the months of maximum rainfall: the annual  
548 peak in rainfall in these locations occurs when the ITCZ is equatorward of them.

549 Based on these common features, we propose that these regions constitute a particular climate type  
550 or regime, underpinned by common dynamics. Analyses in Sections 4 to 7 support this thesis.  
551 In this work, we observe and explain two asymmetries in the annual cycle of observed tropical  
552 precipitation. The first asymmetry is spatial: why do tropical regions with their primary season of  
553 rainfall in autumn systematically lie along eastern coastlines? This spatial pattern can be attributed  
554 to the presence of meridionally oriented mountain ranges that shield these regions from the summer  
555 monsoon westerlies and facilitate orographic ascent during other seasons, including autumn, when  
556 the prevailing winds are easterly. The second is the temporal asymmetry between autumn and  
557 spring: although the prevailing winds are easterly and the surface humidity is high in several of  
558 these regions during local spring, they receive significantly less rainfall in spring than in autumn.

559 This, in all cases, is related to the difference in local atmospheric stability at these times of year: we  
560 find that conditions are more favorable for moist convection in autumn than in spring, attributable  
561 in part to the effect of local SSTs but also to the remote influence of the seasonal cycle of upwelling  
562 in the equatorial Pacific and Atlantic oceans.

563 The use of relative SST as a metric in this context allows us to interpret the effects of the large-  
564 scale coupled tropical ocean-atmosphere system on local precipitation. While relative SST-based  
565 metrics have been used widely in studying tropical cyclone activity and interannual variability, this  
566 is the first use of such a metric, to our knowledge, in understanding the annual cycle of tropical  
567 precipitation.

568 The annual cycle of wind over the equatorial Pacific and Atlantic Oceans in the modern climate  
569 is such that equatorial and coastal upwelling in the eastern parts of these basins are both most  
570 vigorous and of largest spatial extent during boreal autumn, resulting in large swaths of cool SSTs  
571 that reduce the tropical-mean SST. This implies that over the rest of the tropics, this is the most  
572 favorable time of year for deep convection: a conclusion further supported by the peak tropical  
573 cyclone season in many Northern Hemisphere regions occurring during boreal autumn. Idealized  
574 aquaplanet studies examining the asymmetry of tropical precipitation between autumn and spring  
575 (Xian and Miller 2008; Wei and Bordoni 2018) have concluded that the asymmetry arises due to  
576 the high heat capacity of the ocean, which results in a lag of a few months between the timing of  
577 maximum insolation and maximum SST, causing the ITCZ to linger in the autumn hemisphere. A  
578 similar explanation was put forward by studies with realistic continents (Chang et al. 2005; Wang  
579 and Chang 2008). However, we find that the highest SSTs in the annual cycle of many autumn  
580 monsoon regions occur in spring rather than fall, indicating factors other than ocean heat capacity,  
581 such as ocean dynamics or cloud radiative effects, significantly affect the annual cycle of SSTs.  
582 Our results suggest an alternative hypothesis for why more rainfall occurs in boreal autumn than

583 spring, given the modern configuration of continents and insolation, with a key role played by  
584 upwelling in the equatorial cold tongue regions of the Pacific and Atlantic basins.

585 This raises the possibility that the timing of the annual precipitation peak in many autumn monsoon  
586 regions may be sensitive to changes in properties of the cold tongue regions. In past climates with  
587 a different configuration of continents or orbital forcing, this may have resulted in an altered annual  
588 cycle of upwelling (e.g. Bush 1999; Fedorov et al. 2006; Arbuszewski et al. 2013) and therefore  
589 of precipitation in many of these regions. This would also imply that under anthropogenic climate  
590 change, the precipitation in these regions will depend not only on changes in the seasonal cycle of  
591 local SSTs but also on that of the eastern upwelling zones.

592 Here we showed that several mechanistic arguments are consistent with observations of the climatic  
593 seasonal cycle of the atmosphere and ocean; further work is needed to rigorously test these  
594 ideas by perturbing relevant processes in idealized and realistic models. Examining the observed  
595 interannual variations and historical trends in these autumn monsoon regions may also further  
596 advance understanding. Nevertheless, the results presented here eliminate several hypotheses for  
597 the seasonal cycle seen in autumn monsoon regions, such as the idea that it is produced primarily  
598 by local SST or by the seasonal cycle of low-level zonal winds interacting with orography. Perhaps  
599 more importantly, this work identifies a previously unrecognized climate regime that appears in  
600 eastern coastal regions around the globe.

601 *Acknowledgments.* This work was supported by the U.S. Department of Energy, Office of Science,  
602 Biological and Environmental Research under Award Number DE-SC0019367 and by National  
603 Science Foundation Award AGS-1746160.

604 *Data availability statement.* The datasets analyzed in this study are openly available at locations  
605 cited in the reference section.

606    **References**

- 607    Aceituno, P., M. del Rosario Prieto, M. E. Solari, A. Martínez, G. Poveda, and M. Falvey, 2009:  
608         The 1877–1878 el niñ o episode: associated impacts in south america. *Climatic Change*, **92 (3-4)**,  
609         389–416.
- 610    Aldrian, E., and R. D. Susanto, 2003: Identification of three dominant rainfall regions within  
611         indonesia and their relationship to sea surface temperature. *International Journal of Climatology:*  
612         *A Journal of the Royal Meteorological Society*, **23 (12)**, 1435–1452.
- 613    Alpert, P., and H. Shafir, 1989: Mesoscale distribution of orographic precipitation: Numerical  
614         study and comparison with precipitation derived from radar measurements. *Journal of applied*  
615         *meteorology*, **28 (10)**, 1105–1117.
- 616    Amante, C., and B. Eakins, 2009: Etopo1 1 arc-minute global relief model: Procedures, data  
617         sources and analysis. *Memorandum NESDIS NGDC-24*.
- 618    Aparicio, J., P. F. Martínez-Austria, A. Güitrón, and A. I. Ramírez, 2009: Floods in tabasco,  
619         mexico: a diagnosis and proposal for courses of action. *Journal of Flood Risk Management*,  
620         **2 (2)**, 132–138.
- 621    Arbuszewski, J. A., P. B. Demenocal, C. Cléroux, L. Bradtmiller, and A. Mix, 2013: Meridional  
622         shifts of the atlantic intertropical convergence zone since the last glacial maximum. *Nature*  
623         *Geoscience*, **6 (11)**, 959–962.
- 624    Bagtasa, G., 2017: Contribution of tropical cyclones to rainfall in the philippines. *Journal of*  
625         *Climate*, **30 (10)**, 3621–3633.

- 626 Beck, H. E., N. E. Zimmermann, T. R. McVicar, N. Vergopolan, A. Berg, and E. F. Wood, 2018:  
627 Present and future köppen-geiger climate classification maps at 1-km resolution. *Scientific Data*,  
628 **5** (1), doi:10.1038/sdata.2018.214, URL <https://doi.org/10.1038/sdata.2018.214>.
- 629 Bush, A. B., 1999: Assessing the impact of mid-holocene insolation on the atmosphere-ocean  
630 system. *Geophysical Research Letters*, **26** (1), 99–102.
- 631 Chang, C., Z. Wang, J. Ju, and T. Li, 2004: On the relationship between western maritime continent  
632 monsoon rainfall and enso during northern winter. *Journal of Climate*, **17** (3), 665–672.
- 633 Chang, C.-P., Z. Wang, J. McBride, and C.-H. Liu, 2005: Annual cycle of southeast asia—maritime  
634 continent rainfall and the asymmetric monsoon transition. *Journal of climate*, **18** (2), 287–301.
- 635 Chen, T.-C., J.-D. Tsay, M.-C. Yen, and J. Matsumoto, 2012: Interannual variation of the late fall  
636 rainfall in central vietnam. *Journal of Climate*, **25** (1), 392–413.
- 637 Davis, M., 2002: *Late Victorian holocausts: El Niño famines and the making of the third world*.  
638 Verso Books.
- 639 Fedorov, A., P. Dekens, M. McCarthy, A. Ravelo, P. DeMenocal, M. Barreiro, R. Pacanowski,  
640 and S. Philander, 2006: The pliocene paradox (mechanisms for a permanent el niño). *Science*,  
641 **312** (5779), 1485–1489.
- 642 Funk, C., and Coauthors, 2015: The climate hazards infrared precipitation with stations—a new  
643 environmental record for monitoring extremes. *Scientific data*, **2** (1), 1–21.
- 644 Gadgil, S., 2018: The monsoon system: Land–sea breeze or the itcz? *Journal of Earth System  
645 Science*, **127** (1), 1.
- 646 Gamoyo, M., C. Reason, and D. Obura, 2015: Rainfall variability over the east african coast.  
647 *Theoretical and Applied Climatology*, **120** (1-2), 311–322.

- 648 Giannini, A., R. Saravanan, and P. Chang, 2004: The preconditioning role of tropical atlantic  
649 variability in the development of the enso teleconnection: Implications for the prediction of  
650 nordeste rainfall. *Climate Dynamics*, **22** (8), 839–855.
- 651 Greenfield, G. M., 2001: The realities of images: imperial brazil and the great drought. *Transactions*  
652 *of the American Philosophical Society*, **91** (1), ii–148.
- 653 Grossman, R. L., and D. R. Durran, 1984: Interaction of Low-Level Flow with the Western Ghat  
654 Mountains and Offshore Convection in the Summer Monsoon. *Monthly Weather Review*, **112** (4),  
655 652–672, doi:10.1175/1520-0493(1984)112<0652:IOLFW>2.0.CO;2.
- 656 Guha-Sapir, D., R. Below, and P. Hoyois, 2016: Em-dat: the cred/ofda international disaster  
657 database. <https://www.emdat.be/>.
- 658 Hastenrath, S., 2012: Exploring the climate problems of brazil's nordeste: a review. *Climatic*  
659 *Change*, **112** (2), 243–251.
- 660 Hastenrath, S., D. Polzin, and C. Mutai, 2011: Circulation mechanisms of kenya rainfall anomalies.  
661 *Journal of Climate*, **24** (2), 404–412.
- 662 Hersbach, H., and Coauthors, 2020: The era5 global reanalysis. *Quarterly Journal of the Royal*  
663 *Meteorological Society*.
- 664 Houze, R. A., Jr, 2012: Orographic effects on precipitating clouds. *Reviews of Geophysics*, **50** (1).
- 665 Hu, Y., D. Li, and J. Liu, 2007: Abrupt seasonal variation of the ITCZ and the hadley circulation.  
666 *Geophysical Research Letters*, **34** (18), doi:10.1029/2007gl030950.
- 667 Huffman, G. J., and Coauthors, 2007: The trmm multisatellite precipitation analysis (tmpa):  
668 Quasi-global, multiyear, combined-sensor precipitation estimates at fine scales. *Journal of hy-  
669 drometeorology*, **8** (1), 38–55.

- 670 Hung, C.-w., X. Liu, and M. Yanai, 2004: Symmetry and asymmetry of the asian and australian  
671 summer monsoons. *Journal of Climate*, **17** (12), 2413–2426.
- 672 Izumo, T., J. Vialard, M. Lengaigne, and I. Suresh, 2020: Relevance of relative sea surface  
673 temperature for tropical rainfall interannual variability. *Geophysical Research Letters*, **47** (3),  
674 e2019GL086182, doi:10.1029/2019GL086182.
- 675 Johnson, N. C., and S.-P. Xie, 2010: Changes in the sea surface temperature threshold for tropical  
676 convection. *Nature Geoscience*, **3** (12), 842–845.
- 677 Kirshbaum, D. J., B. Adler, N. Kalthoff, C. Barthlott, and S. Serafin, 2018: Moist orographic  
678 convection: Physical mechanisms and links to surface-exchange processes. *Atmosphere*, **9** (3),  
679 80.
- 680 Kripalani, R., and P. Kumar, 2004: Northeast monsoon rainfall variability over south peninsular  
681 india vis-à-vis the indian ocean dipole mode. *International Journal of Climatology: A Journal  
682 of the Royal Meteorological Society*, **24** (10), 1267–1282.
- 683 Kumar, P., K. R. Kumar, M. Rajeevan, and A. K. Sahai, 2006: On the recent strengthening of the  
684 relationship between ENSO and northeast monsoon rainfall over south asia. *Climate Dynamics*,  
685 **28** (6), 649–660, doi:10.1007/s00382-006-0210-0.
- 686 Kumaran, T. V., O. Murali, and S. R. Senthamarai, 2020: Chennai floods 2005, 2015: Vulnerability,  
687 risk and climate change. *Urban Health Risk and Resilience in Asian Cities*, Springer, 73–100.
- 688 Li, T., and S. Philander, 1997: On the seasonal cycle of the equatorial atlantic ocean. *Journal of  
689 climate*, **10** (4), 813–817.
- 690 Li, T., and S. G. H. Philander, 1996: On the annual cycle of the eastern equatorial pacific. *Journal  
691 of Climate*, **9** (12), 2986–2998.

- 692 Liebmann, B., and C. A. Smith, 1996: Description of a complete (interpolated) outgoing longwave  
radiation dataset. *Bulletin of the American Meteorological Society*, **77** (6), 1275–1277.
- 694 Lyon, B., 2003: Enhanced seasonal rainfall in northern venezuela and the extreme events of  
695 december 1999. *Journal of Climate*, **16** (13), 2302–2306.
- 696 Lyon, B., and D. G. DeWitt, 2012: A recent and abrupt decline in the east african long rains.  
697 *Geophysical Research Letters*, **39** (2).
- 698 Medina, S., R. A. Houze Jr., A. Kumar, and D. Niyogi, 2010: Summer monsoon convection in the  
699 himalayan region: terrain and land cover effects. *Quarterly Journal of the Royal Meteorological  
700 Society*, **136** (648), 593–616, doi:10.1002/qj.601.
- 701 Nobre, P., and J. Shukla, 1996: Variations of sea surface temperature, wind stress, and rainfall over  
702 the tropical atlantic and south america. *Journal of Climate*, **9** (10), 2464–2479, doi:10.1175/  
703 1520-0442(1996)009<2464:VOSSTW>2.0.CO;2.
- 704 Pezzi, L., and I. Cavalcanti, 2001: The relative importance of enso and tropical atlantic sea surface  
705 temperature anomalies for seasonal precipitation over south america: a numerical study. *Climate  
706 Dynamics*, **17** (2-3), 205–212.
- 707 Portig, W., 1965: Central american rainfall. *Geographical Review*, **55** (1), 68–90.
- 708 Pulwarty, R. S., R. G. Barry, and H. Riehl, 1992: Annual and seasonal patterns of rainfall variability  
709 over venezuela (jährliche und jahreszeitliche muster der niederschlagsvariabilität in venezuela).  
710 *Erdkunde*, 273–289.
- 711 Ramage, C., J. Marshall, and R. Plumb, 1971: *Monsoon Meteorology*, International Geophysics  
712 Series, Vol. 15. Academic Press.

- 713 Ramsay, H. A., and A. H. Sobel, 2011: Effects of relative and absolute sea surface temperature  
714 on tropical cyclone potential intensity using a single-column model. *Journal of Climate*, **24** (1),  
715 183–193.
- 716 Reynolds, R. W., N. A. Rayner, T. M. Smith, D. C. Stokes, and W. Wang, 2002: An improved  
717 in situ and satellite SST analysis for climate. *Journal of Climate*, **15** (13), 1609–1625, doi:  
718 10.1175/1520-0442(2002)015<1609:aiisas>2.0.co;2.
- 719 Rhea, J. O., and L. Grant, 1974: Topographic influences on snowfall patterns in mountainous  
720 terrain. *Advanced Concepts and Techniques in the Study of Snow and Ice Resources*.
- 721 Robertson, A. W., V. Moron, J.-H. Qian, C.-P. Chang, F. Tangang, E. Aldrian, T. Y. Koh, and  
722 J. Liew, 2011: The maritime continent monsoon. *The global monsoon system: research and*  
723 *forecast*, World Scientific, 85–98.
- 724 Roe, G. H., 2005: Orographic precipitation. *Annual Review of earth and planetary sciences*, **33** (1),  
725 645–671.
- 726 Seager, R., and N. Henderson, 2013: Diagnostic computation of moisture budgets in the era-  
727 interim reanalysis with reference to analysis of cmip-archived atmospheric model data. *Journal*  
728 *of Climate*, **26** (20), 7876–7901.
- 729 Sinclair, M. R., 1994: A diagnostic model for estimating orographic precipitation. *Journal of*  
730 *applied meteorology*, **33** (10), 1163–1175.
- 731 Singh, N., and N. Sontakke, 1999: On the variability and prediction of post-monsoon rainfall over  
732 india. *Int. J. Climatol.*, **19**, 309–39.
- 733 Smith, R. B., 1979: The influence of mountains on the atmosphere. *Advances in geophysics*, **21**,  
734 87–230.

- 735 Smith, R. B., 2018: 100 years of progress on mountain meteorology research. *Meteorological Monographs*, **59**, 20–1.
- 736
- 737 Sobel, A. H., and C. S. Bretherton, 2000: Modeling tropical precipitation in a single column.
- 738 *Journal of climate*, **13 (24)**, 4378–4392.
- 739
- 740 Sobel, A. H., I. M. Held, and C. S. Bretherton, 2002: The enso signal in tropical tropospheric temperature. *Journal of climate*, **15 (18)**, 2702–2706.
- 741
- 742 Suppiah, R., 1989: Relationships between the southern oscillation and the rainfall of sri lanka. *International Journal of Climatology*, **9 (6)**, 601–618.
- 743
- Trewartha, G. T., 1961: *The earth's problem climates*. University of Wisconsin Press.
- 744
- 745 Uvo, C. B., C. A. Repelli, S. E. Zebiak, and Y. Kushnir, 1998: The relationships between tropical pacific and atlantic sst and northeast brazil monthly precipitation. *Journal of Climate*, **11 (4)**, 551–562.
- 746
- 747 van Oldenborgh, G. J., F. E. Otto, K. Haustein, and K. AchutaRao, 2016: The heavy precipitation event of december 2015 in chennai, india. *Bulletin of the American Meteorological Society*, **97 (12)**, S87–S91.
- 748
- 749
- 750 Vecchi, G. A., and B. J. Soden, 2007: Effect of remote sea surface temperature change on tropical cyclone potential intensity. *Nature*, **450 (7172)**, 1066–1070.
- 751
- 752 Waliser, D. E., and C. Gautier, 1993: A satellite-derived climatology of the itcz. *Journal of climate*, **6 (11)**, 2162–2174.
- 753
- 754 Wang, B., 1994: Climatic regimes of tropical convection and rainfall. *Journal of Climate*, **7 (7)**, 1109–1118.
- 755

- 756 Wang, Z., and C. Chang, 2008: Mechanism of the asymmetric monsoon transition as simulated in  
757 an agcm. *Journal of climate*, **21** (8), 1829–1836.
- 758 Wei, H.-H., and S. Bordoni, 2018: Energetic constraints on the itcz position in idealized simulations  
759 with a seasonal cycle. *Journal of Advances in Modeling Earth Systems*, **10** (7), 1708–1725.
- 760 Williams, I. N., and C. M. Patricola, 2018: Diversity of enso events unified by convective threshold  
761 sea surface temperature: a nonlinear enso index. *Geophysical Research Letters*, **45** (17), 9236–  
762 9244.
- 763 Xian, P., and R. L. Miller, 2008: Abrupt seasonal migration of the ITCZ into the summer hemi-  
764 sphere. *Journal of the Atmospheric Sciences*, **65** (6), 1878–1895, doi:10.1175/2007jas2367.1.
- 765 Xie, S.-P., H. Xu, N. Saji, Y. Wang, and W. T. Liu, 2006: Role of narrow mountains in large-scale  
766 organization of asian monsoon convection. *Journal of climate*, **19** (14), 3420–3429.
- 767 Yadav, R. K., 2013: Emerging role of indian ocean on indian northeast monsoon. *Climate dynamics*,  
768 **41** (1), 105–116.
- 769 Yang, W., R. Seager, M. A. Cane, and B. Lyon, 2015: The annual cycle of east african precipitation.  
770 *Journal of Climate*, **28** (6), 2385–2404.
- 771 Zhang, S., and B. Wang, 2008: Global summer monsoon rainy seasons. *International Journal of  
772 Climatology*, **28** (12), 1563–1578, doi:10.1002/joc.1659.
- 773 Zubair, L., 2002: El nino–southern oscillation influences on rice production in sri lanka. *Internation-  
774 al Journal of Climatology*, **22** (2), 249–260.
- 775 Zubair, L., S. A. Rao, and T. Yamagata, 2003: Modulation of sri lankan maha rainfall by the indian  
776 ocean dipole. *Geophysical Research Letters*, **30** (2).

777 **LIST OF TABLES**

778 <b>Table 1.</b>	The data sets used in this study. . . . .	37
779 <b>Table 2.</b>	The climatological monthly mean values of each of the terms in the Reynolds 780 decomposition of the moisture convergence (Equation 4) during the climatologi- 781 cal month of maximum precipitation (based on ERA5) in each autumn monsoon 782 region in units of mm/day. Note that positive values indicate convergence (see 783 text). . . . .	38

TABLE 1. The data sets used in this study.

	Data set	Variables Used	Spatial Resolution (degrees)	Vertical levels	Coverage	Time period	Reference
1.	Climate Hazards center InfraRed Precipitation with Station data ( <b>CHIRPS</b> )	Precipitation	0.05	Surface	Land only	1981-2019	Funk et al. (2015)
2.	Tropical Rainfall Measuring Mission Multi-satellite Precipitation Analysis 3B43 ( <b>TRMM</b> )	Precipitation	0.25	Surface	Land and ocean	1998-2019	Huffman et al. (2007)
3.	European Center for Medium-Range Weather Forecasts Re-analysis 5th Generation ( <b>ERA5</b> )	Precipitation, vertical and horizontal velocity, specific humidity, relative humidity, moisture convergence, convective available potential energy (CAPE)	0.25	37 levels	Land and ocean	1979-2013	Hersbach et al. (2020)
4.	ETOPO1 1 Arc-Minute Global Relief Model ( <b>ETOPO</b> )	Surface height	0.02	-	Land and ocean		Amante and Eakins (2009)
5.	National Oceanic and Atmospheric Administration Optimum Interpolation Sea Surface Temperature v2.0 ( <b>OISST</b> )	Sea surface temperature	1	Surface	Ocean only	1982-2019	Reynolds et al. (2002)
6.	National Oceanic and Atmospheric Administration Interpolated Outgoing Longwave Radiation ( <b>NOAA-OLR</b> )	Outgoing Longwave Radiation (OLR)	2.5	Top of Atmosphere	Land and ocean	1975-2019	Liebmann and Smith (1996)

TABLE 2. The climatological monthly mean values of each of the terms in the Reynolds decomposition of the  
 moisture convergence (Equation 4) during the climatological month of maximum precipitation (based on ERA5)  
 in each autumn monsoon region in units of mm/day. Note that positive values indicate convergence (see text).

	Region	Month	$\nabla \cdot \langle \mathbf{u}q \rangle - \nabla \cdot \langle \bar{\mathbf{u}}\bar{q} \rangle$	$\nabla \cdot \langle \mathbf{u}'\bar{q} \rangle$	$\nabla \cdot \langle \bar{\mathbf{u}}q' \rangle$	$\nabla \cdot \langle \mathbf{u}'q' \rangle$
1.	Central America	October	5.24	4.9	-0.08	0.42
2.	Venezuela	October	3.66	4.15	-0.63	0.14
3.	South Asia	November	4.40	4.27	-0.28	0.41
4.	Malay Peninsula	November	4.59	4.33	0.17	0.09
5.	Vietnam	October	3.44	3.30	0.13	0.02
6.	Philippines	November	2.52	2.50	0.06	-0.03
7.	Brazil	April	5.41	4.54	0.39	0.48
8.	Tanzania	April	2.14	2.52	-0.33	-0.06

787 **LIST OF FIGURES**

- Fig. 1.** The climatological fraction of annual rainfall that occurs during the fall and winter months in (a) the Northern Hemisphere (September to February) and (b) the Southern Hemisphere (March to August). Shades of red and orange indicate regions where half or more of the annual rainfall occurs during these months. Gray boxes highlight the eight regions examined in this study, numbered as in the text of Section 3. . . . .

**Fig. 2.** The climatological annual cycle of precipitation (mm/day) averaged over the areas that receive more than half of their annual rainfall in local autumn and winter in (a) the Northern Hemisphere and (b) the Southern Hemisphere. Spatial averaging was performed over the land areas within the boxes indicated in Figure 1 using CHIRPS data with locations receiving less than half of their annual rainfall in autumn and winter excluded. . . . .

**Fig. 3.** The climatological precipitation (mm/day) averaged over late autumn and early winter in each hemisphere (October to December in (a) and April to June in (b)) from TRMM. The gray contour demarcates areas that receive more than half of their annual rainfall in local autumn and winter (September to February in (a) and March to August in (b)); regions that receive more than half of their annual rainfall during spring and summer are stippled. Light gray boxes indicate the regions used for averaging in Sections 6 and 7. . . . .

**Fig. 4.** The climatological month of maximum precipitation at each location from CHIRPS, after a 5-month running mean was applied to the annual cycle. Regions with annual-mean rainfall less than 2 mm/day are indicated in gray. . . . .

**Fig. 5.** The percentile of outgoing longwave radiation (OLR) with respect to the climatological distribution of OLR over the tropics in (a) November and (b) May (colors). An uneven color scale is used to highlight the lower percentiles, which suggest convective activity. Contours of 5 mm/day and 15 mm/day of climatological precipitation are shown for the corresponding months in white. Colored lines in panels (a) and (b) indicate the centroid at each longitude of monthly climatological precipitation during boreal and austral autumn respectively (see legend), with bold orange lines representing the month for which the other variables in each panel are shown. Green boxes indicate the eight autumn monsoon regions. . . . .

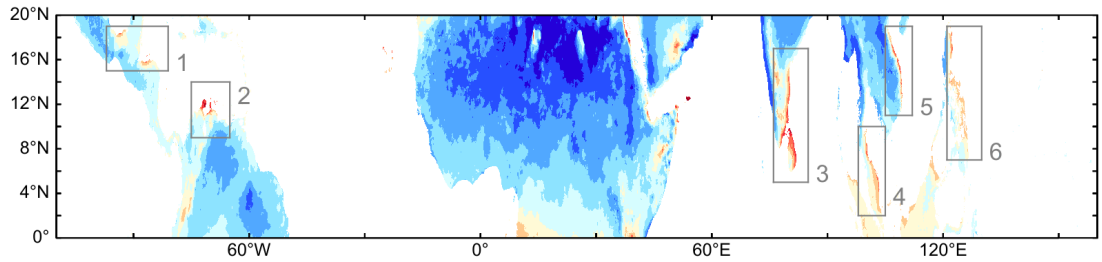
**Fig. 6.** The height of the land surface above sea level (colors) and the climatological seasonal mean wind field at 10 m above the surface (arrows) in (a) October to December in the Northern Hemisphere and (b) April to June in the Southern Hemisphere. . . . .

**Fig. 7.** The climatological precipitation predicted by the orographic model (1st and 3rd columns) and from TRMM (2nd and 4th columns) for comparison in each region, averaged over October–December in the Northern Hemisphere (a-l) and April–June in the Southern Hemisphere (m-p). The red contour demarcates the regions that receive more than half of their annual rainfall in autumn and winter. . . . .

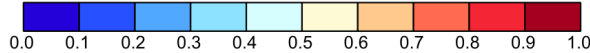
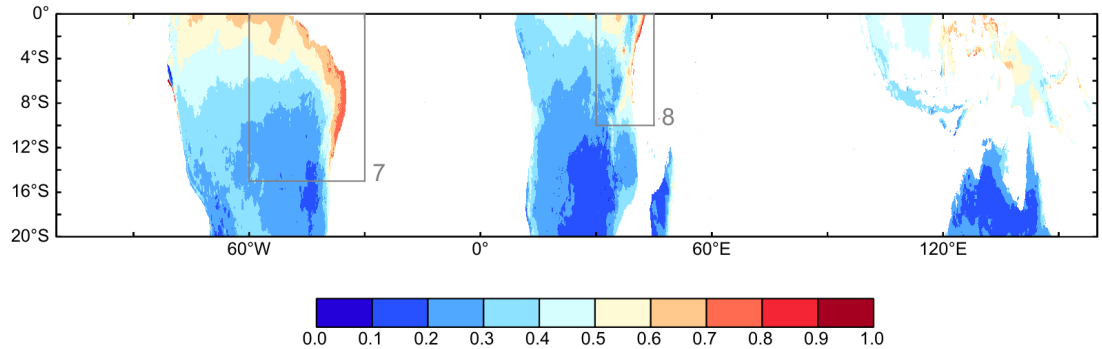
**Fig. 8.** The seasonal cycle of precipitation over autumn monsoon regions predicted by the model of stable upslope ascent, with the surface specific humidity and wind speed in the direction normal to the slope of the surface that were used as inputs. The y-axes for specific humidity (orange, g/kg) and wind speed (green, m/s) are shown on the right. Regions with downslope winds and therefore negative predicted precipitation were set to zero before spatial averaging, and ocean regions were excluded. The dotted lines indicate the month of maximum climatological precipitation in each region from Figure 2. . . . .

830	<b>Fig. 9.</b> The monthly climatologies of precipitation, evaporation, vertically-integrated moisture convergence (VIMC) provided in the reanalysis data, and the VIMC calculated from monthly means from ERA5. The climatological precipitation from TRMM averaged over the same regions is included for comparison. . . . .	49
831		
832		
833		
834	<b>Fig. 10.</b> The climatological annual cycle of the advection, convergence and surface terms calculated in the budget of moisture convergence using ERA5 monthly means for each of the autumn monsoon regions. . . . .	50
835		
836		
837	<b>Fig. 11.</b> The climatological annual cycles of vertical mass flux (colors) and relative humidity as a percentage (contours) averaged over each of the autumn monsoon regions. . . . .	51
838		
839	<b>Fig. 12.</b> The climatological annual cycles of SST and RSST in each of the autumn monsoon regions. The annual-mean SST was subtracted from the climatological values of SST for each region. Panels (a) and (b) are shown with a different y-axis due to the high values of RSST in their annual cycle. The vertical dotted line indicates the month of maximum precipitation over land from Figure 2. . . . .	52
840		
841		
842		
843		
844	<b>Fig. 13.</b> (a) The annual cycle of the tropical-mean SST, averaged between 20°S and 20°N. (b) The difference in climatological SST between autumn and fall, calculated as the September-November mean minus the March-May mean. Negative (blue) values indicate cooler temperatures in boreal autumn.[Need to fix x-axis text in (a)] . . . . .	53
845		
846		
847		

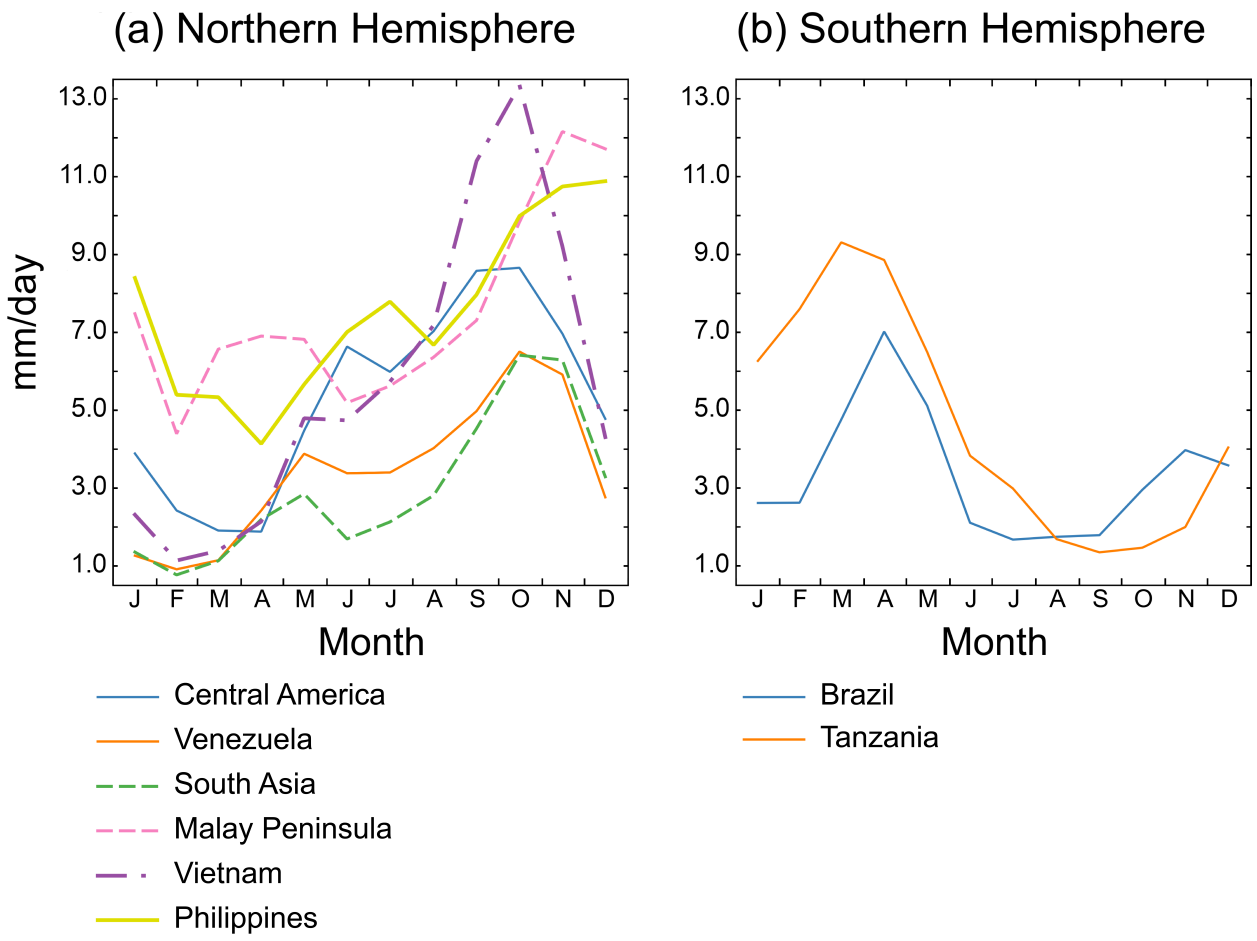
(a) September to February



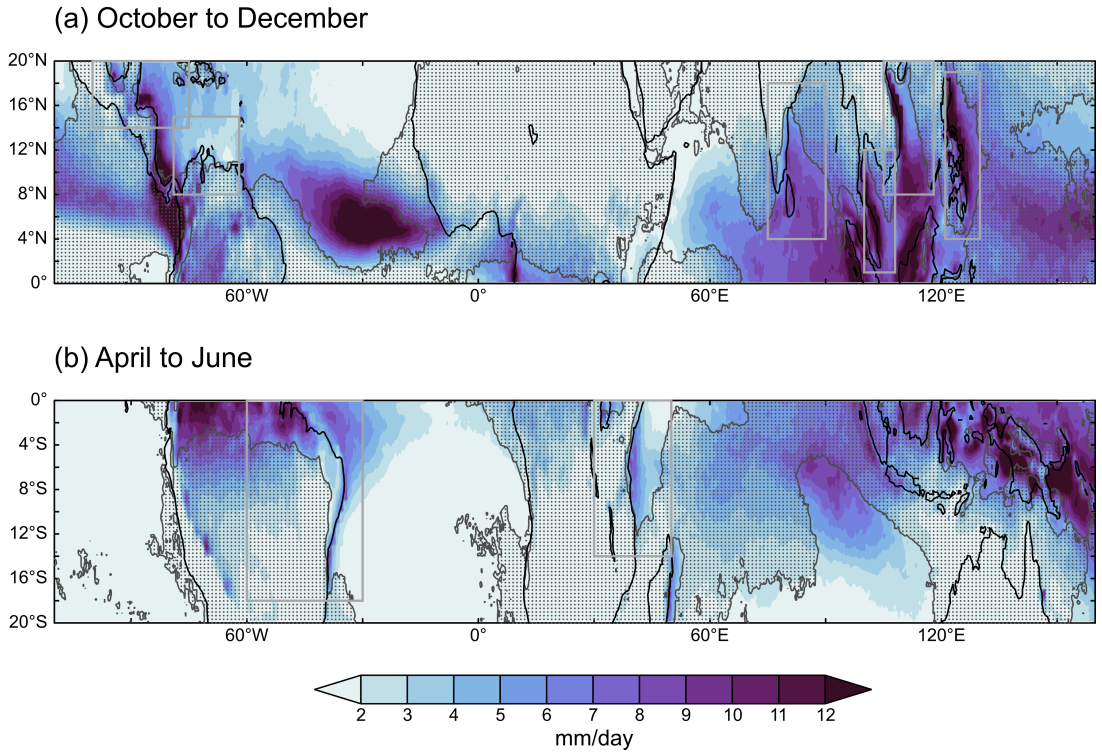
(b) March to August



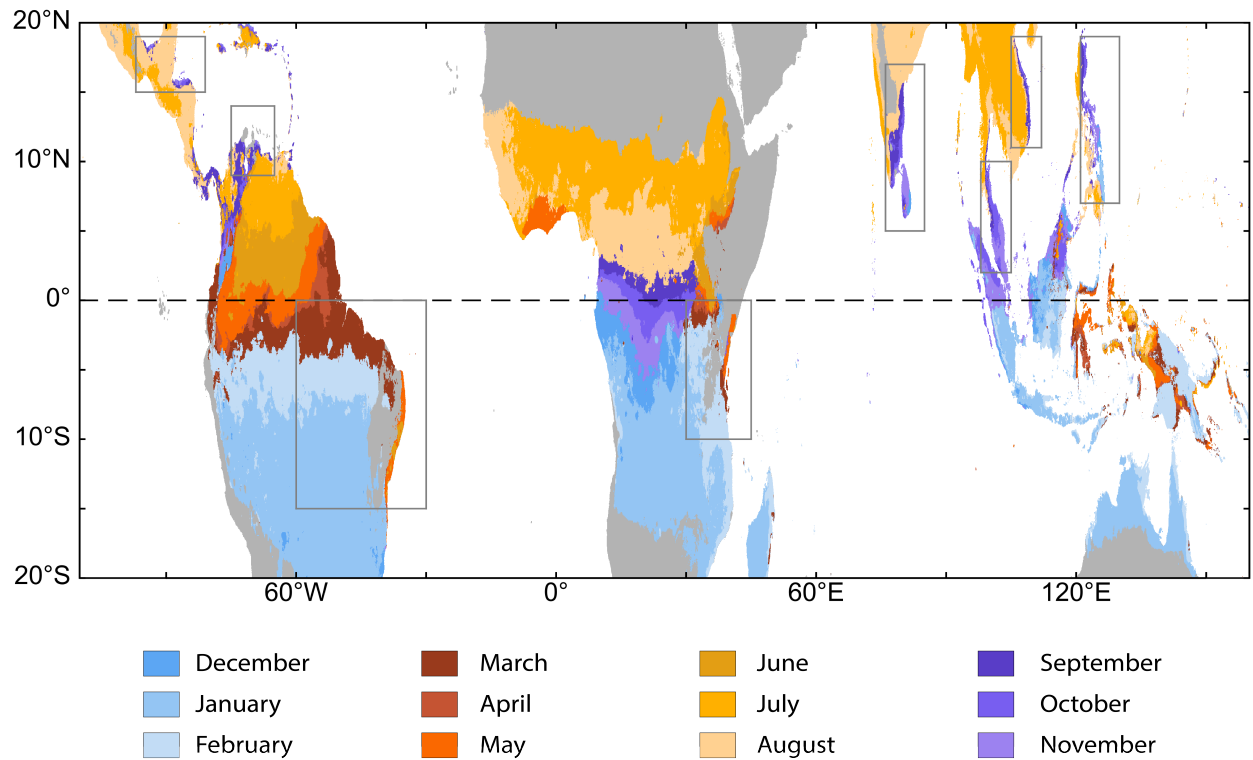
848 FIG. 1. The climatological fraction of annual rainfall that occurs during the fall and winter months in (a) the  
849 Northern Hemisphere (September to February) and (b) the Southern Hemisphere (March to August). Shades  
850 of red and orange indicate regions where half or more of the annual rainfall occurs during these months. Gray  
851 boxes highlight the eight regions examined in this study, numbered as in the text of Section 3.



852 FIG. 2. The climatological annual cycle of precipitation (mm/day) averaged over the areas that receive more  
 853 than half of their annual rainfall in local autumn and winter in (a) the Northern Hemisphere and (b) the Southern  
 854 Hemisphere. Spatial averaging was performed over the land areas within the boxes indicated in Figure 1 using  
 855 CHIRPS data with locations receiving less than half of their annual rainfall in autumn and winter excluded.



856 FIG. 3. The climatological precipitation (mm/day) averaged over late autumn and early winter in each  
 857 hemisphere (October to December in (a) and April to June in (b)) from TRMM. The gray contour demarcates  
 858 areas that receive more than half of their annual rainfall in local autumn and winter (September to February in  
 859 (a) and March to August in (b)); regions that receive more than half of their annual rainfall during spring and  
 860 summer are stippled. Light gray boxes indicate the regions used for averaging in Sections 6 and 7.



861 FIG. 4. The climatological month of maximum precipitation at each location from CHIRPS, after a 5-month  
 862 running mean was applied to the annual cycle. Regions with annual-mean rainfall less than 2 mm/day are  
 863 indicated in gray.

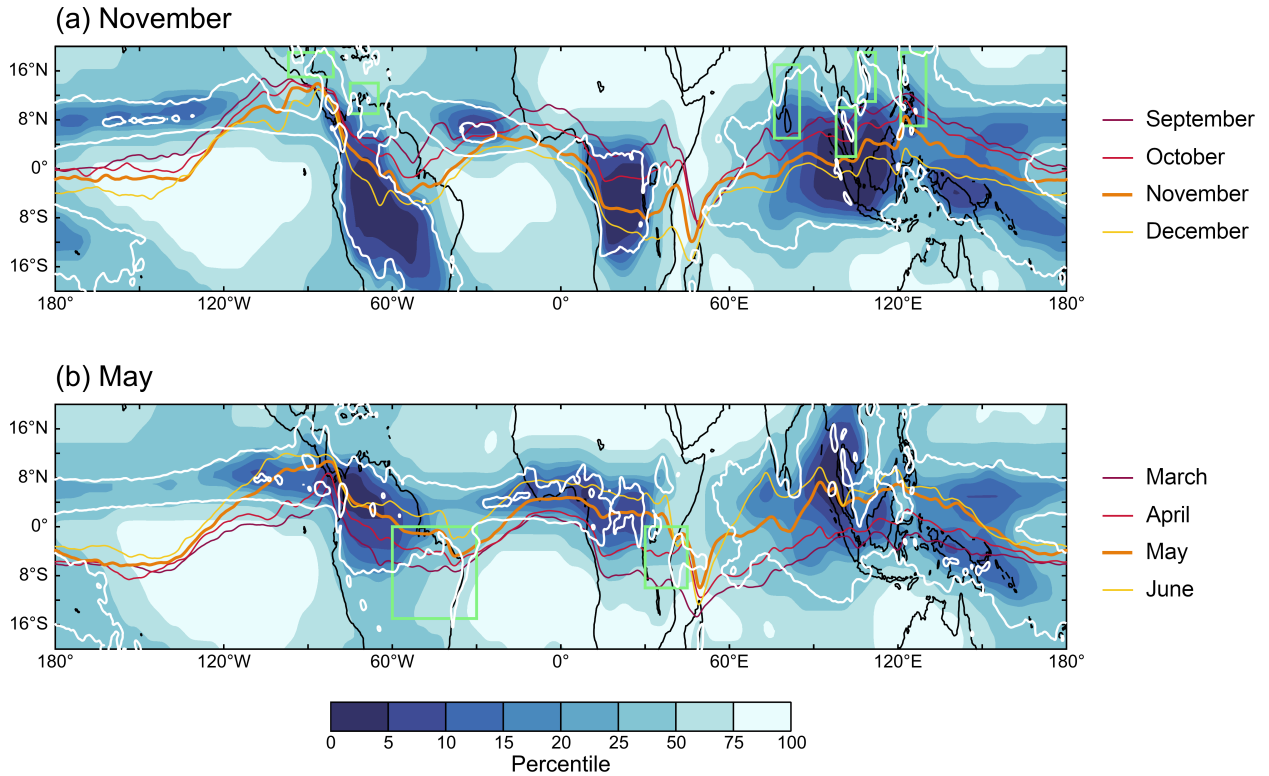
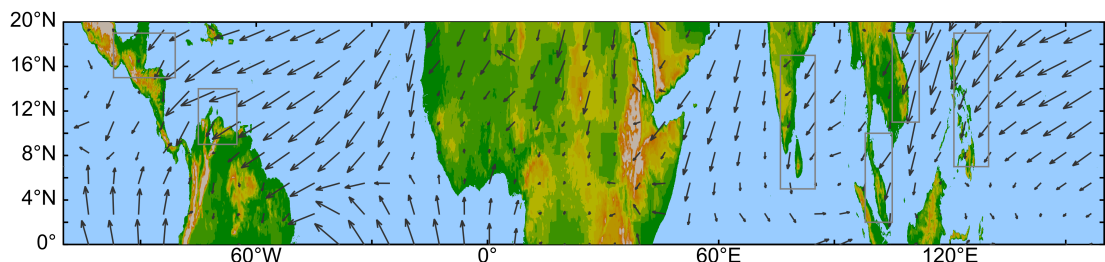
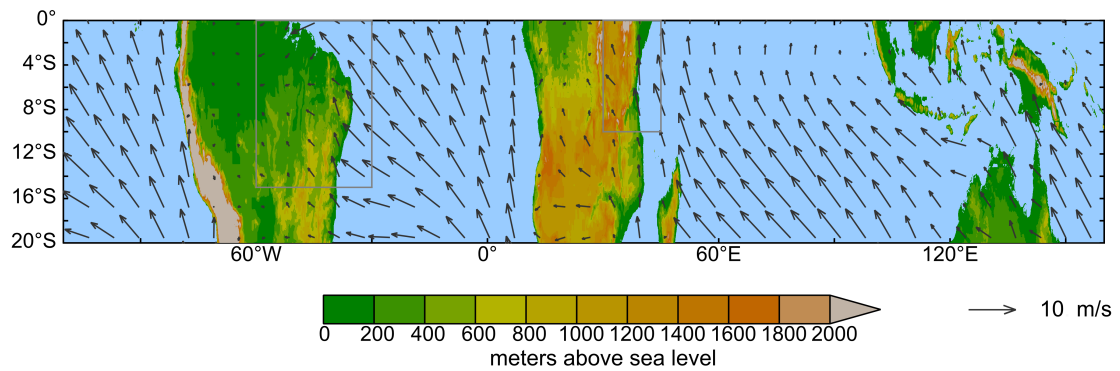


FIG. 5. The percentile of outgoing longwave radiation (OLR) with respect to the climatological distribution of OLR over the tropics in (a) November and (b) May (colors). An uneven color scale is used to highlight the lower percentiles, which suggest convective activity. Contours of 5 mm/day and 15 mm/day of climatological precipitation are shown for the corresponding months in white. Colored lines in panels (a) and (b) indicate the centroid at each longitude of monthly climatological precipitation during boreal and austral autumn respectively (see legend), with bold orange lines representing the month for which the other variables in each panel are shown. Green boxes indicate the eight autumn monsoon regions.

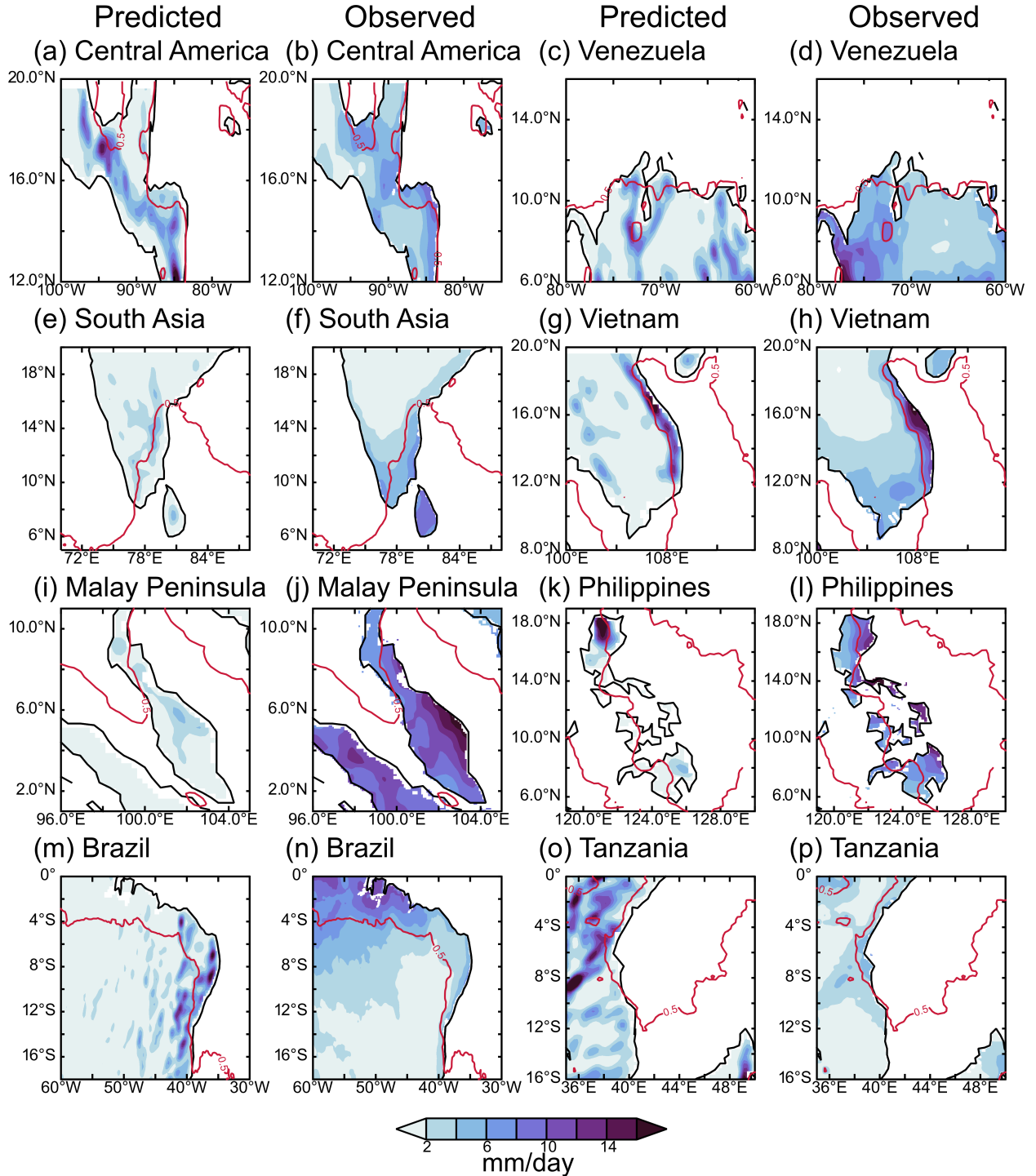
(a) October to December



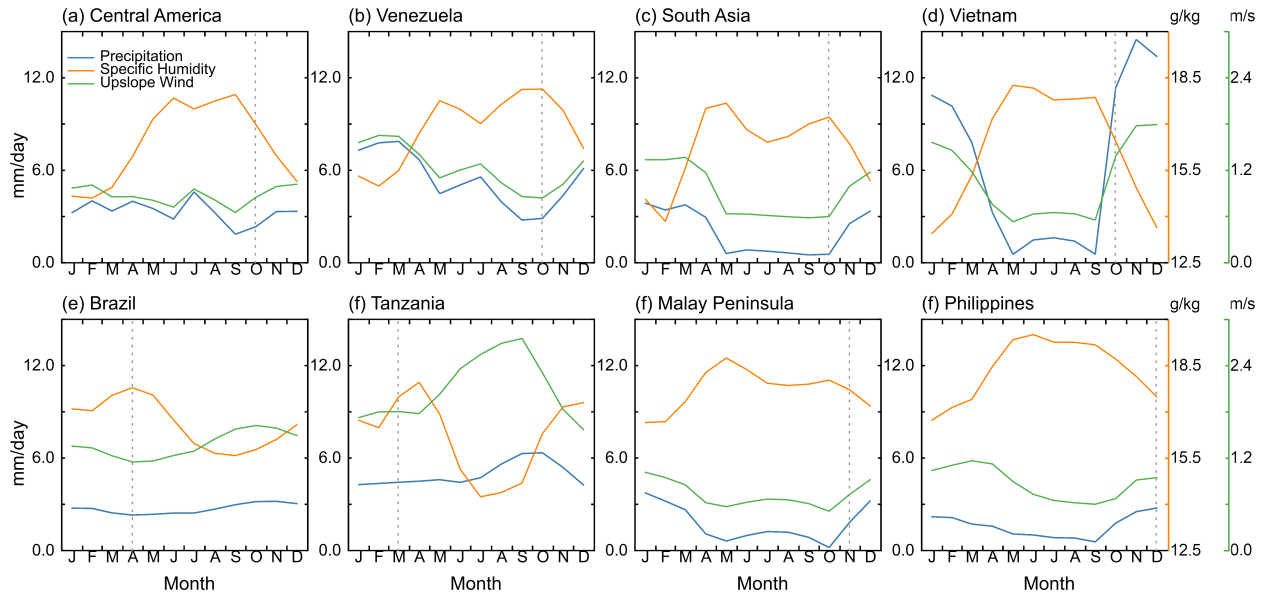
(b) April to June



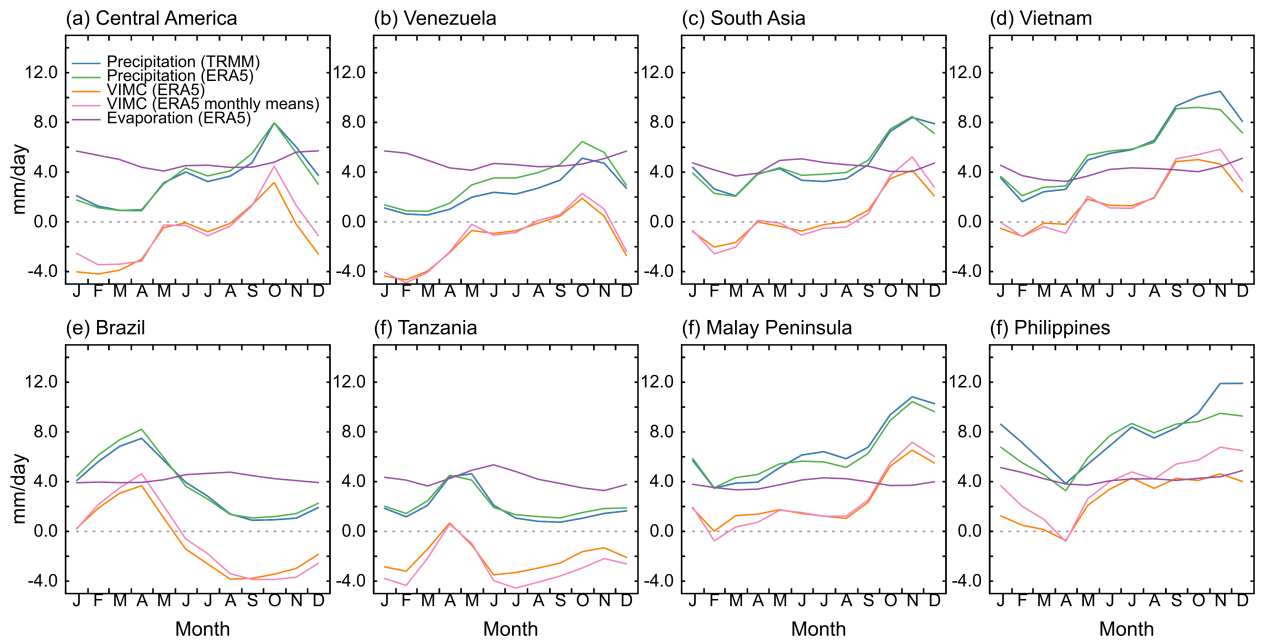
871 FIG. 6. The height of the land surface above sea level (colors) and the climatological seasonal mean wind field  
872 at 10 m above the surface (arrows) in (a) October to December in the Northern Hemisphere and (b) April to June  
873 in the Southern Hemisphere.



874     FIG. 7. The climatological precipitation predicted by the orographic model (1st and 3rd columns) and from  
875     TRMM (2nd and 4th columns) for comparison in each region, averaged over October-December in the Northern  
876     Hemisphere (a-l) and April-June in the Southern Hemisphere (m-p). The red contour demarcates the regions  
877     that receive more than half of their annual rainfall in autumn and winter.



878 FIG. 8. The seasonal cycle of precipitation over autumn monsoon regions predicted by the model of stable  
 879 upslope ascent, with the surface specific humidity and wind speed in the direction normal to the slope of the  
 880 surface that were used as inputs. The y-axes for specific humidity (orange, g/kg) and wind speed (green, m/s)  
 881 are shown on the right. Regions with downslope winds and therefore negative predicted precipitation were set to  
 882 zero before spatial averaging, and ocean regions were excluded. The dotted lines indicate the month of maximum  
 883 climatological precipitation in each region from Figure 2.



884      FIG. 9. The monthly climatologies of precipitation, evaporation, vertically-integrated moisture convergence  
 885      (VIMC) provided in the reanalysis data, and the VIMC calculated from monthly means from ERA5. The  
 886      climatological precipitation from TRMM averaged over the same regions is included for comparison.

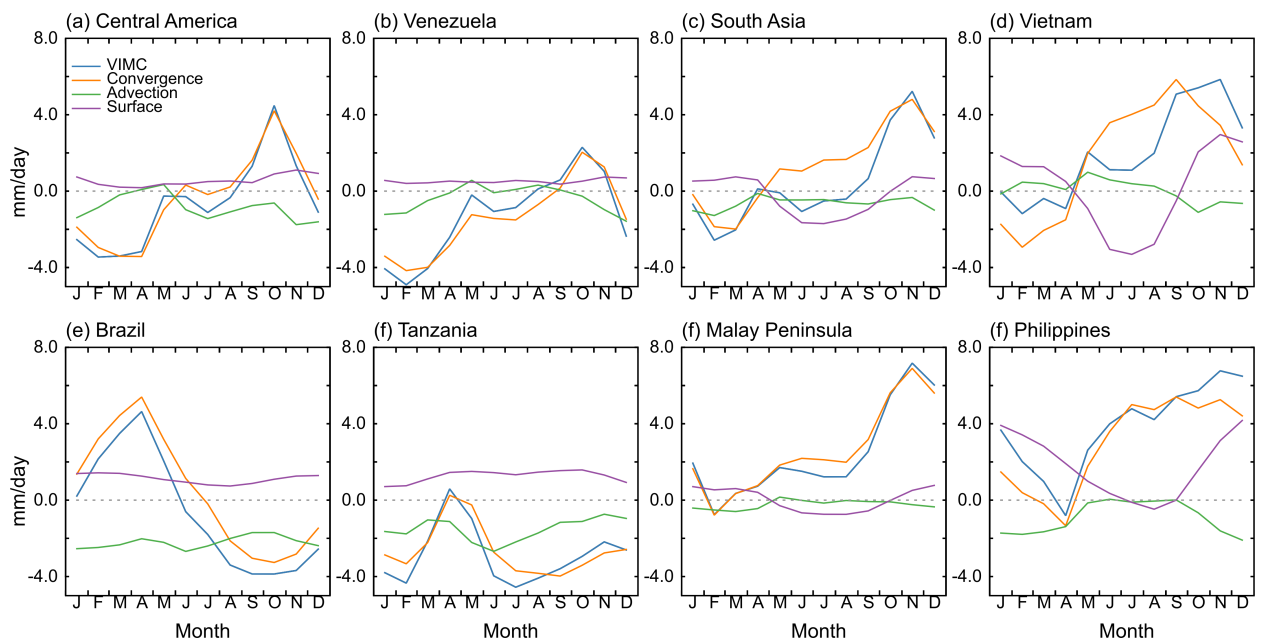
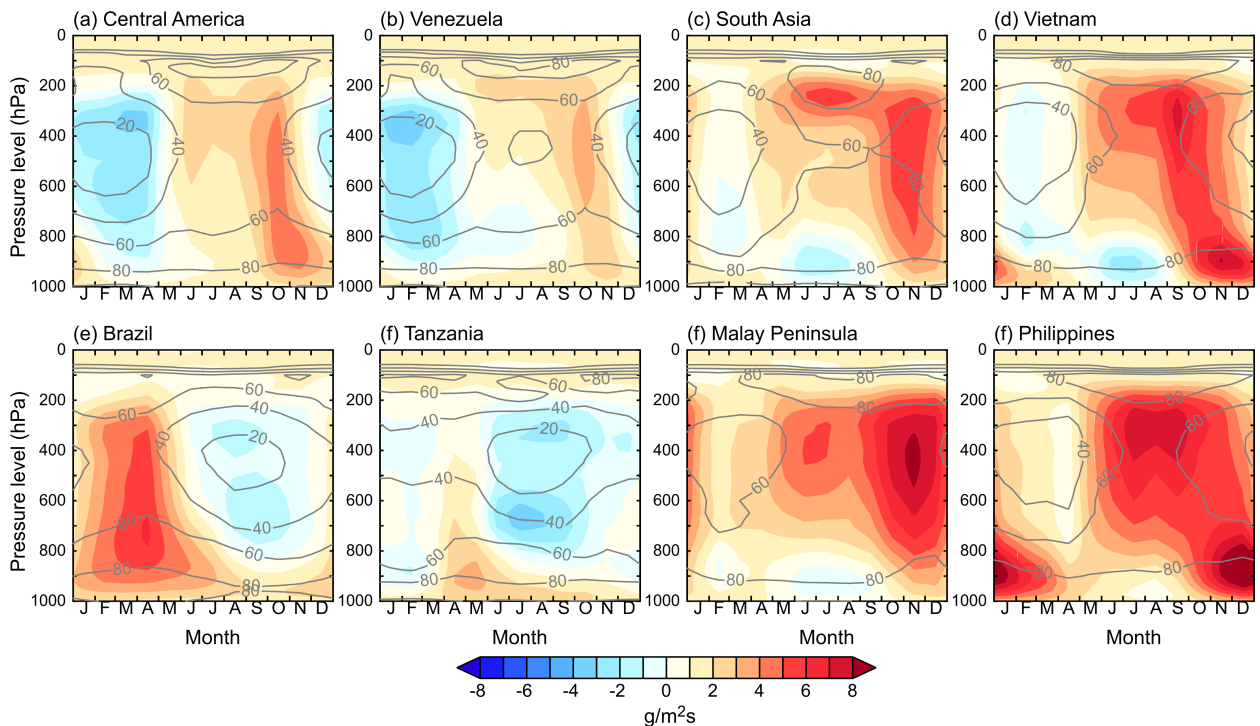
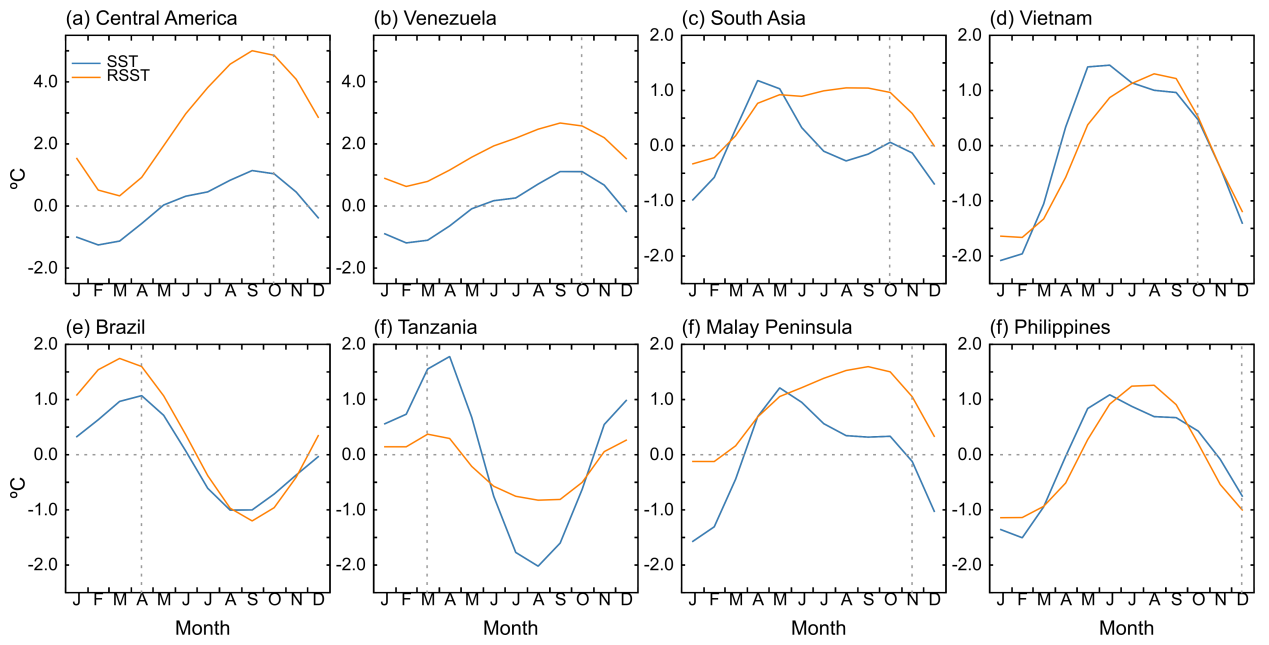


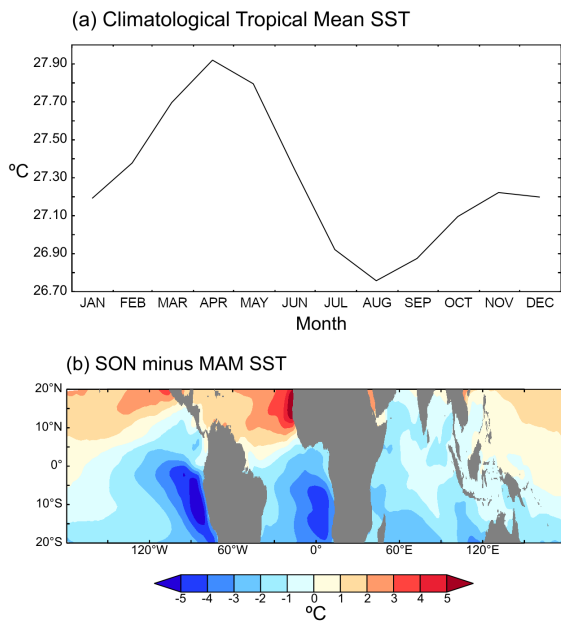
FIG. 10. The climatological annual cycle of the advection, convergence and surface terms calculated in the budget of moisture convergence using ERA5 monthly means for each of the autumn monsoon regions.



889 FIG. 11. The climatological annual cycles of vertical mass flux (colors) and relative humidity as a percentage  
 890 (contours) averaged over each of the autumn monsoon regions.



891 FIG. 12. The climatological annual cycles of SST and RSST in each of the autumn monsoon regions. The  
 892 annual-mean SST was subtracted from the climatological values of SST for each region. Panels (a) and (b) are  
 893 shown with a different y-axis due to the high values of RSST in their annual cycle. The vertical dotted line  
 894 indicates the month of maximum precipitation over land from Figure 2.



895 FIG. 13. (a) The annual cycle of the tropical-mean SST, averaged between 20°S and 20°N. (b) The difference in  
 896 climatological SST between autumn and fall, calculated as the September-November mean minus the March-May  
 897 mean. Negative (blue) values indicate cooler temperatures in boreal autumn.[Need to fix x-axis text in (a)]